NASA/TM—2015-218811 DOT/FAA/TC–15/22

Dynamic Open-Rotor Composite Shield Impact Test Report

Silvia Seng and Charles Frankenberger
Naval Air Warfare Center Weapons Division, China Lake, California

Charles R. Ruggeri, Duane M. Revilock, J. Michael Pereira, and Kelly S. Carney
Glenn Research Center, Cleveland, Ohio

William C. Emmerling
FAA William J. Hughes Technical Center, Atlantic City International Airport, New Jersey

November 2015

NASA STI Program . . . in Profile

Since its founding, NASA has been dedicated to the advancement of aeronautics and space science. The NASA Scientific and Technical Information (STI) Program plays a key part in helping NASA maintain this important role.

The NASA STI Program operates under the auspices of the Agency Chief Information Officer. It collects, organizes, provides for archiving, and disseminates NASA's STI. The NASA STI Program provides access to the NASA Technical Report Server—Registered (NTRS Reg) and NASA Technical Report Server—Public (NTRS) thus providing one of the largest collections of aeronautical and space science STI in the world. Results are published in both non-NASA channels and by NASA in the NASA STI Report Series, which includes the following report types:

- TECHNICAL PUBLICATION. Reports of completed research or a major significant phase of research that present the results of NASA programs and include extensive data or theoretical analysis. Includes compilations of significant scientific and technical data and information deemed to be of continuing reference value. NASA counter-part of peer-reviewed formal professional papers, but has less stringent limitations on manuscript length and extent of graphic presentations.

- TECHNICAL MEMORANDUM. Scientific and technical findings that are preliminary or of specialized interest, e.g., "quick-release" reports, working papers, and bibliographies that contain minimal annotation. Does not contain extensive analysis.

- CONTRACTOR REPORT. Scientific and technical findings by NASA-sponsored contractors and grantees.

- CONFERENCE PUBLICATION. Collected papers from scientific and technical conferences, symposia, seminars, or other meetings sponsored or co-sponsored by NASA.

- SPECIAL PUBLICATION. Scientific, technical, or historical information from NASA programs, projects, and missions, often concerned with subjects having substantial public interest.

- TECHNICAL TRANSLATION. English-language translations of foreign scientific and technical material pertinent to NASA's mission.

For more information about the NASA STI program, see the following:

- Access the NASA STI program home page at http://www.sti.nasa.gov

- E-mail your question to help@sti.nasa.gov

- Fax your question to the NASA STI Information Desk at 757-864-6500

- Telephone the NASA STI Information Desk at 757-864-9658

- Write to:
  NASA STI Program
  Mail Stop 148
  NASA Langley Research Center
  Hampton, VA 23681-2199

NASA/TM—2015-218811 DOT/FAA/TC–15/22

Dynamic Open-Rotor Composite Shield Impact Test Report

Silvia Seng and Charles Frankenberger
Naval Air Warfare Center Weapons Division, China Lake, California

Charles R. Ruggeri, Duane M. Revilock, J. Michael Pereira, and Kelly S. Carney
Glenn Research Center, Cleveland, Ohio

William C. Emmerling
FAA William J. Hughes Technical Center, Atlantic City International Airport, New Jersey

National Aeronautics and
Space Administration

Glenn Research Center
Cleveland, Ohio 44135

November 2015

Level of Review: This material has been technically reviewed by technical management.

Available from

NASA STI Program
Mail Stop 148
NASA Langley Research Center
Hampton, VA 23681-2199

National Technical Information Service
5285 Port Royal Road
Springfield, VA 22161
703-605-6000

This report is available in electronic form at http://www.sti.nasa.gov/ and http://ntrs.nasa.gov/

Dynamic Open-Rotor Composite Shield Impact Test Report

Silvia Seng and Charles Frankenberger
Naval Air Warfare Center Weapons Division
China Lake, California 93555

Charles R. Ruggeri, Duane M. Revilock, J. Michael Pereira, and Kelly S. Carney
National Aeronautics and Space Administration
Glenn Research Center
Cleveland, Ohio 44135

William C. Emmerling
FAA William J. Hughes Technical Center
Atlantic City International Airport, New Jersey 08405

Summary

The Federal Aviation Administration (FAA) is working with the European Aviation Safety Agency to determine the certification base for proposed new engines that would not have a containment structure on large commercial aircraft. Equivalent safety to the current fleet is desired by the regulators, which means that loss of a single fan blade will not cause hazard to the aircraft. NASA Glenn and Naval Air Warfare Center (NAWC) China Lake collaborated with the FAA Aircraft Catastrophic Failure Prevention Program to design and test a shield that would protect the aircraft passengers and critical systems from a released blade that could impact the fuselage. This report documents the live-fire test from a full-scale rig at NAWC China Lake. NASA provided manpower and photogrammetry expertise to document the impact and damage to the shields. The test was successful: the blade was stopped from penetrating the shield, which validates the design analysis method and the parameters used in the analysis. Additional work is required to implement the shielding into the aircraft.

1.0 Introduction

The Federal Aviation Administration (FAA) is working with the European Aviation Safety Agency to determine the certification base for new engines being proposed for large commercial aircraft that would not have a containment structure. Regulators want the new systems to have safety equivalent to that of the current fleet, meaning that the loss of a single fan blade will not cause a hazard to the aircraft. One method to achieve this is to provide a shield that would protect passengers and the aircraft's critical systems from a released blade that could impact the fuselage. To evaluate the feasibility of this concept, engineers from the NASA Glenn Research Center and the Naval Air Warfare Center (NAWC) China Lake collaborated with the FAA Aircraft Catastrophic Failure Prevention Program to design and test a composite shield that could provide the required protection. The test was conducted in February 2014 by the Naval Air Warfare Center Weapons Division (NAWCWD) Weapons Survivability Lab (WSL) on behalf of the FAA Aircraft Catastrophic Failure Prevention Program. The purpose of the test was to evaluate the effectiveness of composite panels in preventing penetration of the aircraft fuselage by an open-rotor aircraft engine blade. Glenn engineers designed and analyzed the composite shields and the test configuration and provided photogrammetry expertise, equipment, and analysis support. The LS–DYNA explicit finite element code (Livermore Software Technology Corp., Livermore, CA) was used for the shield impact analysis. NAWCWD WSL conducted the test and provided the test hardware.

Based on an analysis performed by NASA (Ref. 1), two shield thicknesses were tested, 20 and 24 ply. The blades were predicted to penetrate the 20-ply composite material, but not the 24-ply composite material. Two blades, similar in size and construction to that expected for open-rotor engines on a

midsize commercial aircraft, were mounted on a spin fixture and run at a representative velocity. Using a linear shape charge, the two blade sections were released simultaneously so that they would impact the composite shields. The test was designed to duplicate the worst-case scenario; that is, the blades were released at a high-power-climb rotor speed, with both blade sections impacting tip first and with the blade aligned with the trajectory of the center of gravity (CG) of each blade. The test was conducted successfully, and the results were consistent with the NASA analysis predictions: The thinner shield was penetrated by the blade, and the thicker shield prevented penetration. This report documents the live-fire test from the full-scale rig at NAWC China Lake, describes the damage to the shields, and presents the instrumentation results. Test results are reported in the units they were measured in.

1.1 Background

In the 1980s, aircraft engine manufacturers began to investigate new engine design concepts to improve fuel efficiency because of rising fuel costs resulting from the oil embargo in 1973, the revolution in Iran, and the Iran-Iraq war. One of the concepts was an open-rotor unducted turbofan. Open-rotor engines may have the potential to reduce the specific fuel consumption by as much as 25 percent or more. Two main open-rotor concepts were developed with the goal of achieving an engine that would be able to provide comparable aircraft speeds to a ducted turbofan at much greater efficiencies (Ref. 2). Pratt & Whitney, Hamilton Standard, and Allison teamed up to offer the 578–DX, a geared propfan with counterrotating blades. The General Electric (GE) unducted fan (UDF) also used two sets of counterrotating blades (Fig. 1). Rather than a traditional stator-rotor turbine, the GE UDF engine was designed with counterrotating turbines as well, each one providing power to one set of UDF blades.

Two major technical challenges—significant noise generation and exposure to uncontained propeller debris—had not been solved in earlier designs. These challenges and reduced fuel prices resulted in decreased interest to develop the open-rotor design concept in the 1980s.

Current increased fuel costs and greenhouse gas environmental concerns have reinvigorated interest in open-rotor and UDF engine designs. The FAA Office of Environment and Energy, NASA, and engine manufacturers have been evaluating new engine designs that utilize two unshrouded counterrotating rows of blades. Significant improvement in engine noise reduction has been achieved by advances in computer modeling for blade design and use of composite materials for open-rotor blades.

Use of advanced composites in fuselage structures may address airplane threats from uncontained blade failures. This report documents results of testing to validate the effectiveness of composite panels for shielding the fuselage from debris.

The open-rotor engine design concept does not fall under existing regulations for either turboprop or turbofan engine installation. The fan blades are mounted external to the engine flow path, and there are many more blades than there are on a turboprop. The renewed interest in the development of open-rotor

Figure 1.—General Electric (GE) unducted fan demonstrator.

engines and unducted turbofan engine designs has led the FAA to investigate the feasibility of fuselage shielding for protection in the event of a blade release. The goal of the FAA is for open-rotor engines to have an equivalent level of safety as current ducted fan engines where loss of a single blade is not a hazardous event.

The FAA initiated an open-rotor shield research program that consisted of the following sequence of events:

1. NASA performed penetration tests on high-damage-tolerance braided composite materials (Ref. 3).
2. NAWCWD conducted generic open-rotor-engine aircraft studies to show the benefits of a composite shielding material (App. A).
3. NASA conducted detailed shield penetration analyses to investigate the feasibility of composite shielding (Ref. 1).
4. NAWCWD fabricated and tested a composite shield design (this report).
5. NAWCWD conducted a cross engine debris trade study (App. B).

Glenn engineers conducted analyses and small-scale testing to predict the thickness needed for a composite material to stop a released fan blade. The aircraft geometry used for the analyses was based on a medium-range, twin-engine, midsize (150-passenger) narrow-body commercial aircraft with a high wing and a wing-mounted open-rotor engine. The open-rotor engine specifications were provided by NAWCWD and the FAA. The configuration incorporated open-rotor, wing-mounted engines as shown in Figure 2. This generic configuration does not address the cross-engine debris certification requirement discussed in Appendix B.

The diameter of an open-rotor engine suitable for this size of an aircraft was to be between 13.1 and 13.8 ft based upon Reference 2. For the test, a 162-in.- (13.5-ft-) diameter rotor was selected based on available test assets and hardware. The horizontal distance between the centerline of the engine and the fuselage centerline was 188 in., with a vertical distance of 85 in.

The analysis was conducted in two parts. In the first part a trajectory analysis was conducted. The aircraft and engine geometries were modeled to determine what release angles would result in the worst-case impacts to the fuselage. The release angles providing a velocity vector perpendicular to the fuselage skin and having the highest impact velocity were found to be a release angle of 30° (blade rotating counterclockwise) or 180° from the top (blade rotating clockwise), as shown in Figure 2. The full details of the analysis are described in Reference 1.

The results of the first part of the analysis were used to determine the position and velocity of the blade just before impact. These parameters were used as inputs to a finite element model for the second part of the analysis. The computational time was reduced by positioning the blade at the predicted position just before impact, rather than beginning at the engine release point. The finite element analysis indicated that a 24-layer (approximately 0.52-inch-thick) T700S/PR520 triaxially braided composite was sufficient to stop the blade from penetrating the shield.

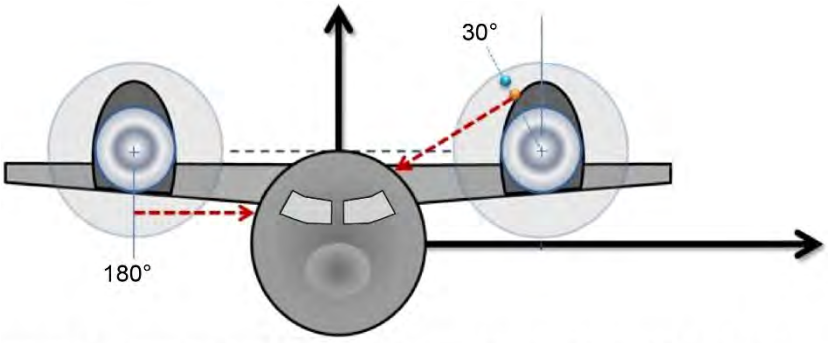

Figure 2.—Open-rotor wing-mounted engine configuration and NASA analysis impact locations.

1.2 Test Objective

The following tasks were to be performed in this test:

1. Release representative blade fragments into two braided composite panels and collect data that can be used to validate the LS–DYNA analysis of composite panels to protect the fuselage from a fan blade-off event.
2. Document the released blade trajectory to obtain data that can be used to validate the NASA trajectory study and answer questions raised by industry on previous large angular trajectory experience.

2.0 Test Article Description

The test involved two main components, the composite fuselage panel and the simulated open-rotor blade.

2.1 Composite Fuselage Panel

Analysis of shielding materials to protect a fuselage from a single blade was conducted by the NASA Glenn Research Center Impact Dynamics Group. The composite fuselage panel built up for this test series was based on the NASA design analysis (Ref. 1). The panel did not contain any stiffeners or stringers. The design concept for the shielding is a floating panel that will not be subject to the flexure of the primary aircraft structure. By isolating the panel from the fuselage structure, the panel is not exposed to those additional stresses and strains and can be made of a lighter weight material than a structural shielding panel.

The composite test panel was a curved 4- by 8-ft section with a radius of curvature of 6.5 ft. Four composite panels were fabricated: two composed of 20 layers of braided carbon fiber prepreg, each resulting in a thickness of approximately 0.45 in., and two composed of 24 layers, each resulting in a thickness of approximately 0.56 in. The material was a prepreg made with a triaxial carbon fiber (T700S) braid from A&P Technology, Inc. (see Fig. 3). The prepreg resin was Cytec MTM45–1 resin (Cytec Industries, Inc.). The resin was chosen because it provides a high-strength, damage-resistant, structural epoxy matrix that can be processed in an autoclave without expensive tooling and was similar to the PR520 used in the analysis. The specifications for the material are shown in Table I.

The composite panels were made by the NAWCWD composite materials shop on tooling designed and built by WSL range engineers and the WSL shop. The composite panel represents the composite barrier only, with no stringers. The panel was supported in a frame that matched the NASA-modeled boundary conditions as closely as possible. The panel mounting structure, described in Section 5.2, was designed to simply support the panel in the three translational directions, allowing rotation along the panel edges.

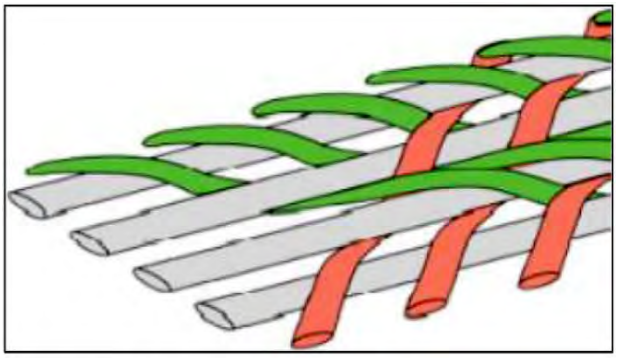

Figure 3.—Triaxial braid pattern of carbon fiber prepreg used for composite shields.

TABLE I.—FEDERAL AVIATION ADMINISTRATION OPEN-ROTOR PROJECT COMPOSITE MATERIAL SPECIFICATIONS

Preform	
A&P product code	QISO–H–52.8–A
Width	52.8 in.
Fiber areal weight	536 gsm
Fiber orientation	0 ± 60°
Directional content	33.3 percent in each orientation
Fiber type	T700SC–12K50C
Prepreg	
Resin	MTM45–1
Resin content	36 wt%
Width	52.8 in.
Process method	Dual film

2.2 Rotor Blade

The fan blades of an open-rotor turbofan are large, adjustable-pitch, unshrouded blades. The design typically features two rows of counter-rotating blades. The unshrouded blades provide greater efficiency than traditional turbofans. Noise issues that hindered the development of these engines in the 1980s have been reduced with the help of advances in computational fluid dynamics (CFD) programs.

The blades used for this testing (see Figs. 4 and 5) were similar in design and materials to those that could be used for open-rotor engines. A modern propeller was used as the surrogate with the outer portion acting as the open-rotor fan blade-off simulation. The blades have a polyurethane foam core, sandwiched between carbon fiber spars, with composite reinforced skins. A thin strip of metal protects the leading edge from small, "nominal," foreign object damage, such as small debris from unimproved runways (see Figs. 4 and 5).

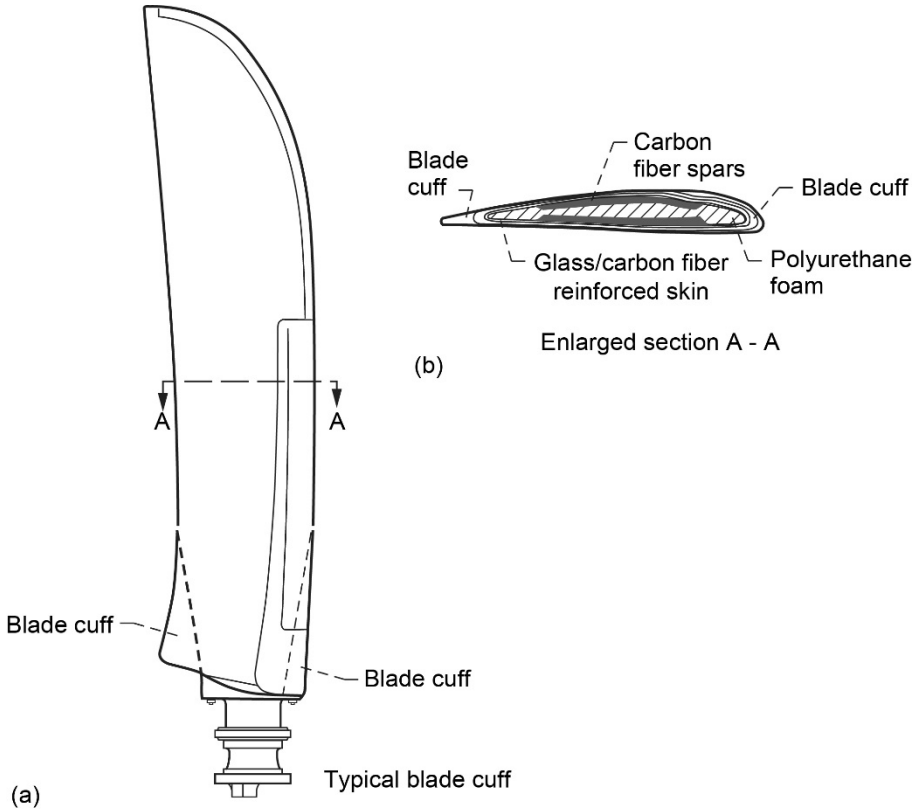

Figure 4.—Typical composite blade for shield impact tests. (a) Full blade. (b) Cross section.

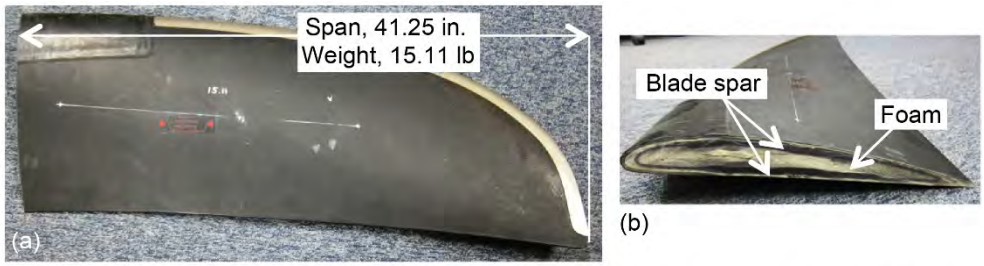

Figure 5.—Candidate blade configuration for shield impact. (a) Outer blade length and weight. (b) Blade cross section.

3.0 Test Approach

A single test event was conducted. Two blades were mounted to the rotor hub and spin rig on the WSL spin fixture, shown in Figure 6. The spin fixture is a T406 engine and gearbox that are capable of providing the 1108 rpm speed required for this test. The two blades were explosively released at 8° past vertical. Two 4- by 8-ft composite panels were located approximately 124 in. from either side of the centerline of the spin fixture, so that they were centered on the predicted blade release trajectories. The fuselage structure was not represented.

Two of the six blades were mounted in the spin rig. Linear shape charges were placed 41.25 in. from the blade tip of each blade. The shape charges were simultaneously initiated to release the blades at the same time.

3.1 Blade Separation Investigations

Prior to the start of testing, a pretest investigation was conducted to validate the ability to cut the blade with minimal damage to surrounding blade structure and imparting minimal force on the resulting blade section. An additional objective for this testing was to assess the potential for damage to the spin fixture and/or damage to the released blade section that may influence test results.

A single blade was fixed to an overhead mounting structure (Fig. 7). The blade was not allowed to rotate. A weight was suspended from the end of the blade. The suspended weight was meant to encourage separation, but was much smaller than the centripetal forces on the blade at 1108 rpm (200 lb for the pretest investigation and over 26 000 lb estimated for the blade in motion).

A witness board was placed adjacent to the blade to represent the spin fixture. The damage to the witness board was used to evaluate the damage from the detonation of the linear shape charge. A 600 grain/ft linear shape charge was placed along the chord of one side of the rotor blade, closest to the

Figure 6.—Spin rig on T406 spin fixture.

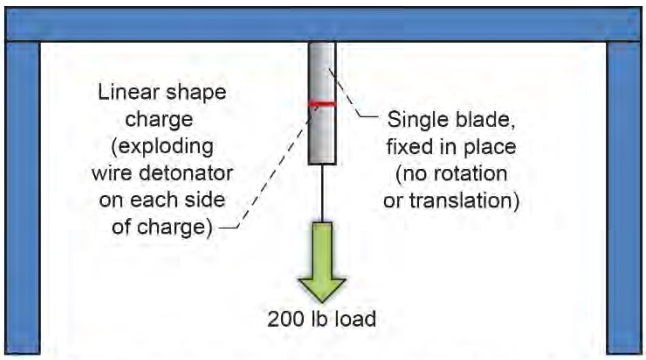

Figure 7.—Test setup to investigate effectiveness of linear shape charge.

witness board. If the shape charge had effectively severed the blade, without significant damage that could influence test results, the test would have been deemed successful. However, the shape charge did not fully sever the blade. The spar adjacent to the linear shape charge was severed, but the opposite spar was intact.

Because the shape charge did not completely sever the blade, the test was repeated with the shape charge cord around the full circumference of the blade (Fig. 8). The second test was performed on the same blade, several inches above the location of the first test. The blade was completely severed by the linear shape charge cord around the full circumference of the blade. The spars appeared to have visibly delaminated some on either side of the linear shape charge. A large piece of the blade trailing edge (aft of the carbon spars) separated from the remaining blade section; however, this appears to be a result of damage from the first test.

Test instrumentation was limited to one high-speed video camera, a safety video, and a firing line. The shape charge resulted in a significant fire ball, but it did not impart significant force on the blade. Figure 9 shows the blade root section rotating as a result of the blast, but does not propel the blade vertically. Likewise, the outer span of the blade merely falls away from the cut. Review of the severed blade section reveals a relatively clean cut with composite delamination reaching approximately 1 in. away from the cut line (Fig. 10).

Figure 8.—Blade with shape charge around full circumference.

Figure 9.—Shape charge detonation, full-circumference configuration.

Figure 10.—Blade section at cut line.

Additional pretesting was done after the T406 spin fixture and test rig were installed onto the test pad. Pretest checkouts included engine runs as well as testing of the linear shape charge firing system. Detonators were placed on the fan blades but not the linear shape charge. The pretest was conducted just as the final full-up test would be, utilizing the same procedure. The flash from the detonators functioning is visible in the high-speed video. The detonator flash provided verification for the timing of the firing signal without damaging the blades and demonstrated the integrity of the firing chain.

The detonators were inserted into a small aluminum cube to secure the detonator and the end of the linear shape during the test. During one of the pretest spin-ups without the detonators installed, the detonator block broke free from the blade and impacted one of the test panels. Although there was no visible damage from the detonator holding block, the panel was replaced. Detonator blocks were then bolted onto the blade to ensure they remained in place.

3.2 Test Pad Setup

The T406 engine was mounted to the WSL engine test stand with the open-rotor fan blade-off test rig attached as shown in Figure 11.

The test pad setup was based on the worst-case trajectories defined by the NASA analysis (Ref. 1). To minimize the height of the fuselage panel fixture, the centerlines of the fuselage and the engines were placed at the same height. This orientation results in a 24° rotation of the coordinate system, centered on the centerline of the fuselage (shown in Fig. 12). Therefore, the release angle of a blade at the 180° orientation (blade oriented straight down) would become 204°. The 30° release angle would become 6° (30 – 24 = 6).

Figure 11.—Open-rotor fan blade-off test rig.

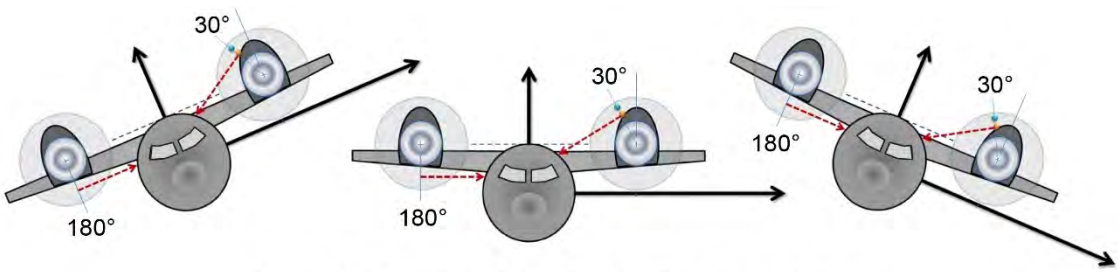

Figure 12.—Rotation of aircraft about fuselage centerline.

The release angle for the test was chosen to be 8°. This was based on the recommendations from NASA to provide the worst-case impact angle for the blades simultaneously released from the hub. The 8° release angle was predicted to result in the tip's first impact with the blade to be aligned with the velocity vector of the blade CG. The composite test panels were placed such that the centerline of the fuselage panels and engine centerline were at the same height. The horizontal distance of the panels from the engine was set to ensure that the distance from the release point CG to the impact on the composite test panels was the same as the distance used by the NASA analysis. The final placement of the panels relative to the engine is illustrated in Figure 13.

The panels were held in a test fixture that replicated the boundary conditions of the NASA analysis as shown in Figures 14 and 15. The panels were fixed in all three translation axes and simply supported on half-round bars that allowed the edges to rotate about the support frame interface (Fig. 15). The panels were restrained along all four edges utilizing 3/8-in. bolts, spaced approximately every 4 in. around the frame, and tightened down with sufficient force to restrain the panel in the translation axis. A rubber gasket was inserted between the restraint bars and the composite panels to minimize stress concentrations in the panels.

The linear shape charge was installed to cut the blade 41.25 in. in from the blade tip. The spin fixture was operated at 1108 rpm to provide the target blade velocity of 527 ft/s. This provided the target blade weight of 15.1 lb and release blade CG of 26 in. from the tip (Table II).

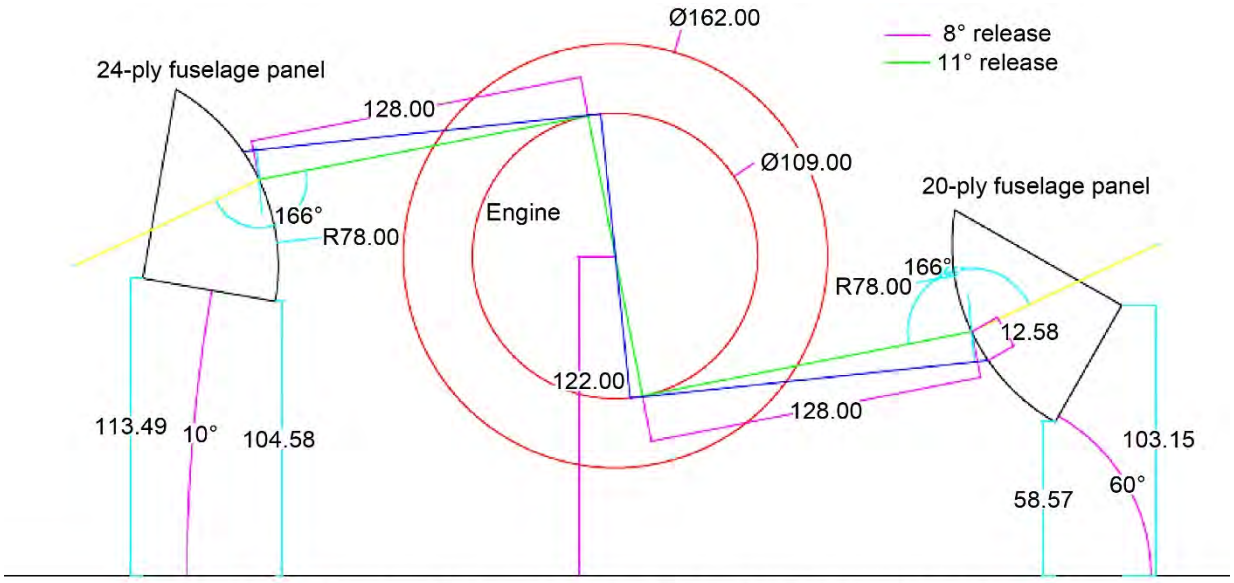

Figure 13.—Engine and fuselage panel setup on test pad. Dimensions are in inches.

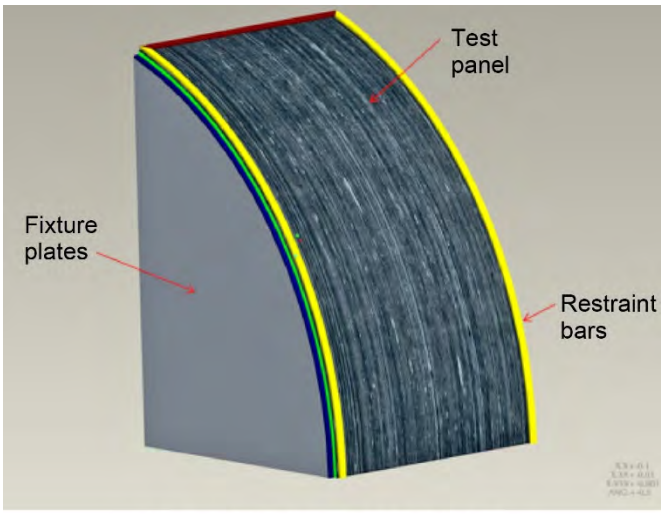

Figure 14.—Panel support fixture.

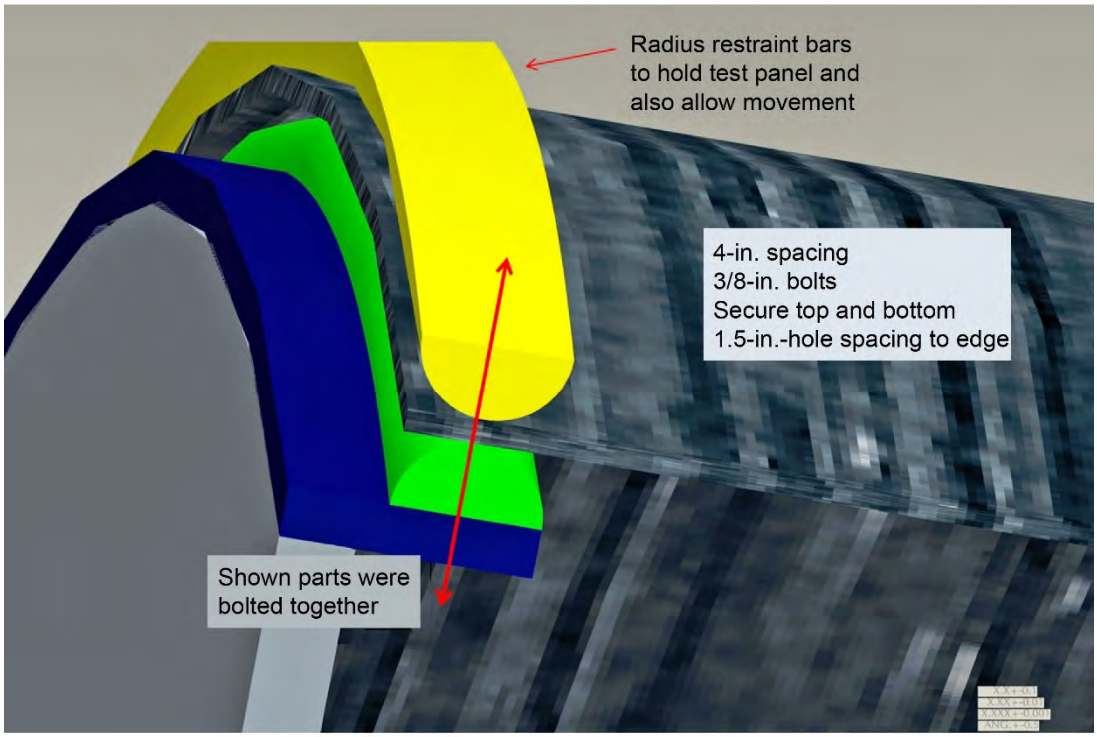

Figure 15.—Panel attachment concept.

Table II.—TARGET BLADE CHARACTERISTICS

Release blade length, in.	41.25
Release blade weight, lb	15.1
Release center of gravity diameter, in.	109
Rotor speed, rpm	1108
Release angle, deg	8
Blade velocity, ft/s	527

3.3 Video Recording

NASA personnel provided cameras for digital image correlation (DIC) and personnel to set up, operate, and provide the analysis for the DIC. The imaging system was the primary data source to evaluate the displacement of the test panels. These data were required to validate the NASA analysis of the composite panels.

The six cameras provided by NASA were operated in pairs. Two cameras were placed behind each test panel to record the blade impact. The third camera pair was placed forward of the test fixture, looking aft, to capture the release of the blade and impact on the composite panel. The cameras were located behind steel blast shields to protect them from debris from the impact of the blade into the panels. Lighting was provided to illuminate the fuselage panels to ensure the maximum frame rate and desired shutter speeds could be achieved. The cameras were placed in fixed positions and calibrated to provide the DIC. The DIC software was used to process video images from which the displacement of the panel was calculated.

Two cameras were provided by the WSL to capture overall views of the test event. One camera was placed in front of the test fixture looking aft, a second high-speed camera was placed aft looking forward. The approximate camera placement is shown in Figures 16 to 18. Additional standard-speed (24 frames/s) video cameras were placed on the test pad at the discretion of the firing officer to monitor safety views of the test pad and to monitor the spin fixture engine.

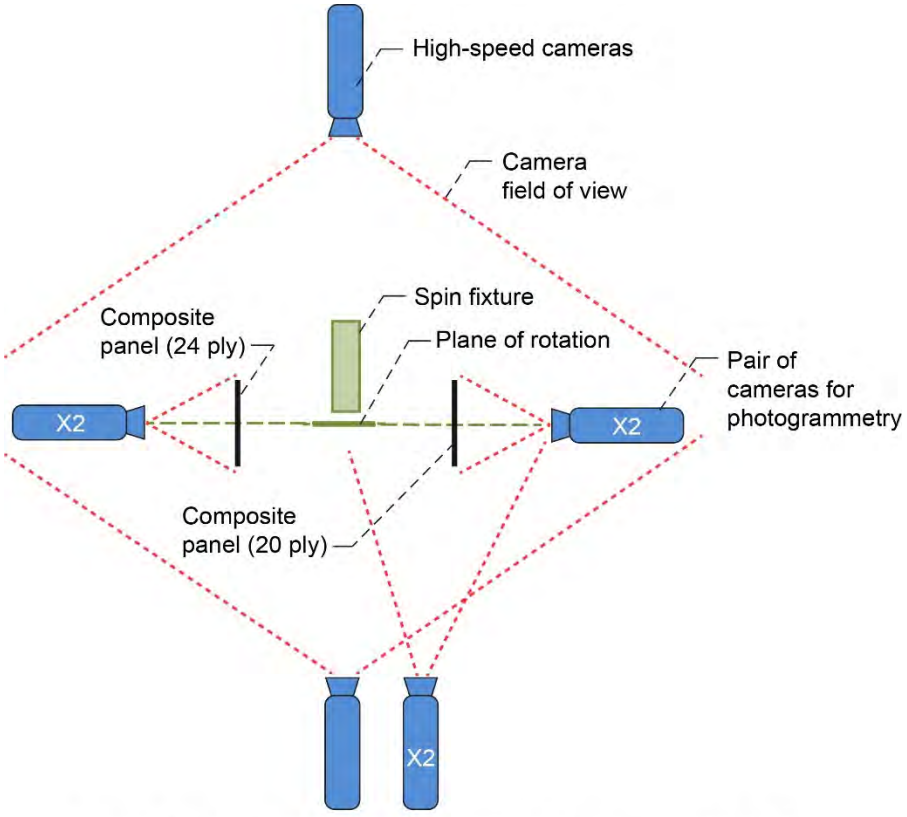

Figure 16.—Test pad high-speed camera configuration (not to scale).

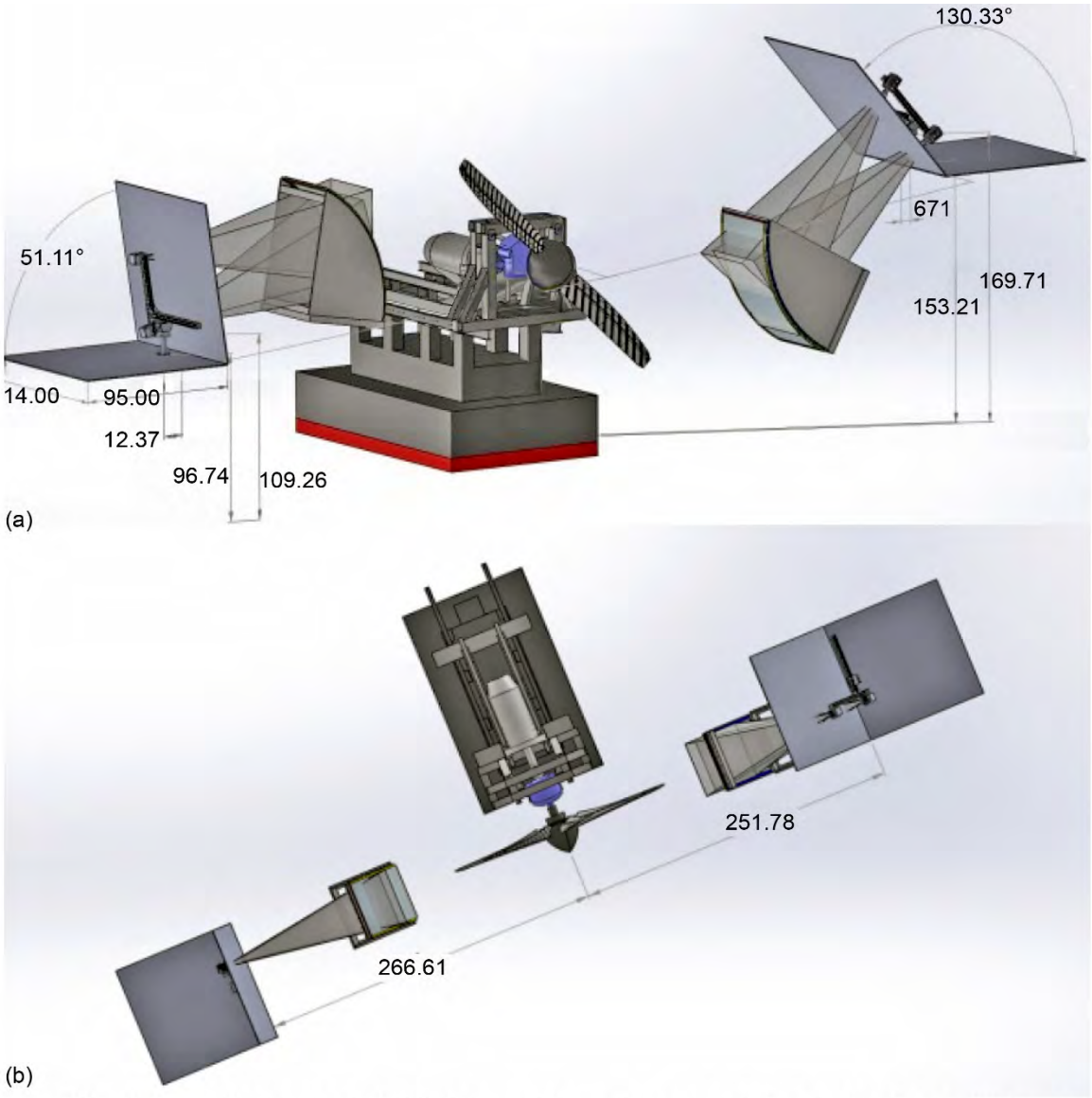

Figure 17.—High-speed camera and shield placement. Dimensions are in inches. (a) Front view. (b) Top view.

Figure 18.—High-speed camera locations for digital image correlation; four cameras, two per panel.

3.4 Instrumentation

High-speed video was used to measure the fan blade time-of-flight. Sensors installed on the spin fixture monitored the health of the engine and measured the spin rig velocity (in rpm). Additional data were provided by 12 accelerometers on the panels and along the restraint bars. The measurements made during the test are listed in Table III.

The accelerometers were installed in the same locations and orientations on each panel support structure; their locations on the 20- and 24-ply panels are shown in Figures 19 and 20, respectively. For each panel, three accelerometers were placed in the lower left corner of the frame (viewed from the concave side of the panel): (1) P20–X1 and P24–X1 for the 20- and 24-ply panels, respectively, are aligned with the fuselage (“x-axis”); (2) P20–Y1 and P24–Y1 are aligned in the tangential (“y-axis”) orientation; and (3) P20–Z1 and P24–Z1 are aligned in the radial (“z-axis”) orientation. Two accelerometers were placed in the lower right corner of the panels (viewed from the concave side of the panel): (1) P20–Y2 and P24–Y2 aligned in the tangential orientation and (2) P20–Z2 and P24–Z2 aligned in the radial orientation. Finally, one accelerometer was placed in the upper left corner: P20–Y3 and P24–Y3 aligned in a near-tangential orientation, as shown in Figure 21. The accelerometers were used to collect backup data to compare with the NASA analysis data. The accelerometer data are presented in Appendix C.

TABLE III.—TEST MEASUREMENTS

Parameter	Units	Data rate
Gas generator speed Power turbine speed Propeller speed	Percent of maximum limit Percent of maximum limit Revolutions per minute (rpm)	20 Hz
Torque Main gearbox temperature Engine fuel flow	Pounds-foot (lb-ft) Degrees Celsius (°C) Gallons per minute (gpm)	20 Hz
Gearbox oil pressure	Pounds per square inch, gauge (psig)	20 Hz
Oil temperature Bearing temperature Bearing temperature	Degrees Fahrenheit (°F)	20 Hz
Zero time signal	Volts (V)	100 kHz
Acceleration, 20-ply panel P20–X1 P20–Y1 P20–Z1 P20–Y2 P20–Z2 P20–Y3	Acceleration of gravity (g)	100 kHz
Acceleration, 24-ply panel P24–X1 P24–Y1 P24–Z1 P24–Y2 P24–Z2 P24–Y3	Acceleration of gravity (g)	100 kHz

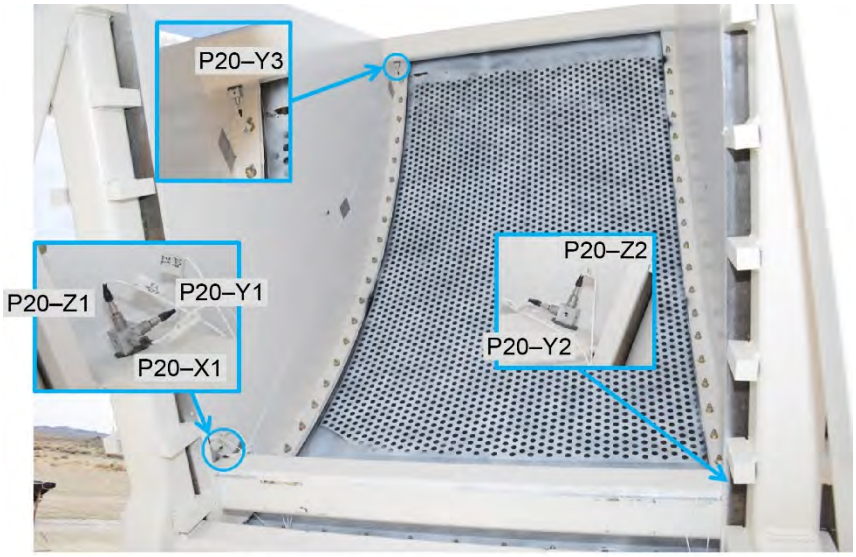

Figure 19.—20-ply panel accelerometer locations.

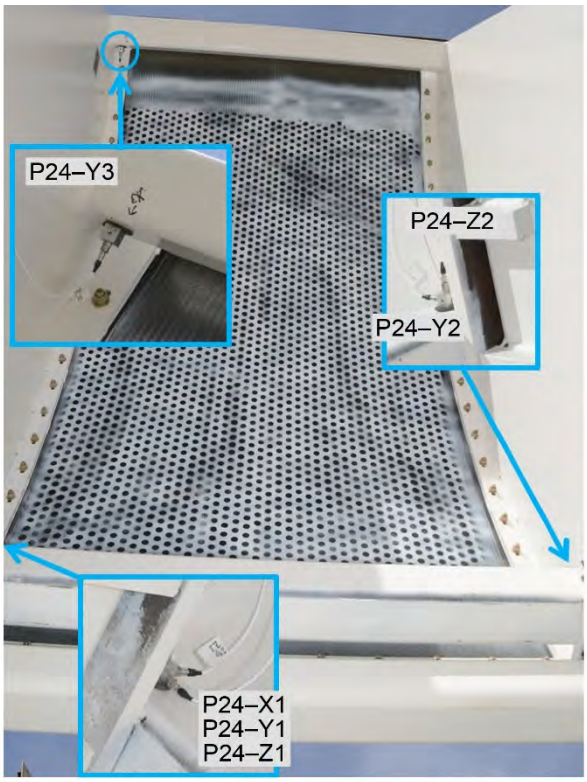

Figure 20.—24-ply panel accelerometer locations.

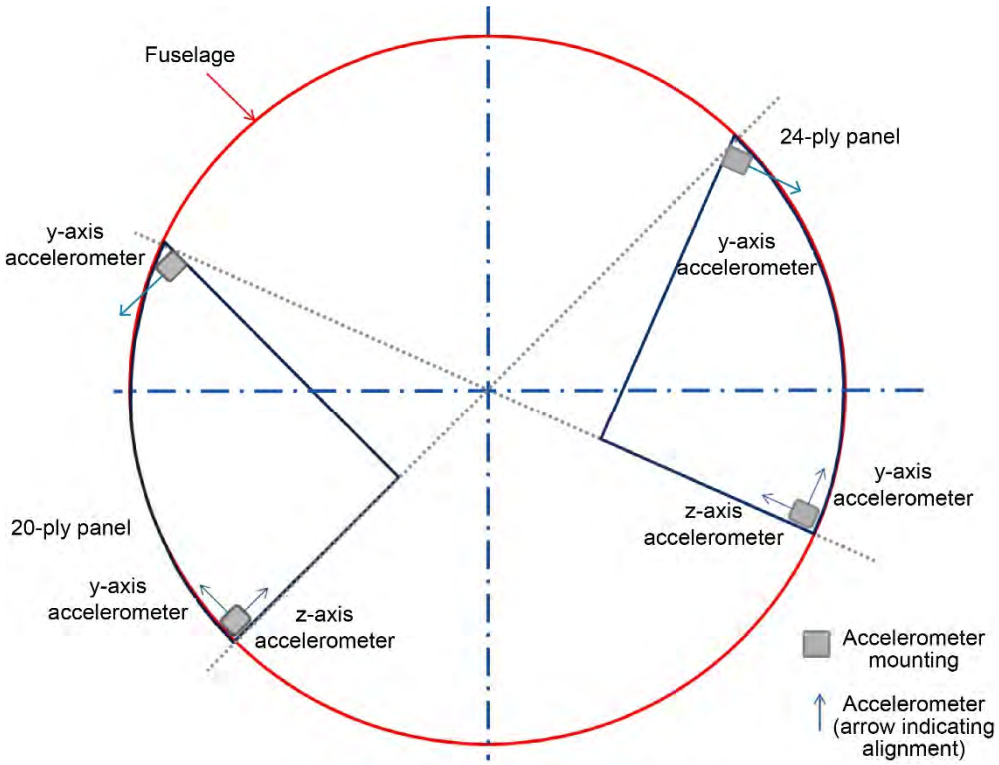

Figure 21.—Accelerometer orientation (not to scale).

3.5 Photogrammetry

Three pairs of high-speed digital video cameras were used to quantitatively measure the full-field deflection of the back side of each test panel as well as the kinematics of one of the released fan blades. The commercial DIC software ARAMIS (GOM mbH, Germany) was used to compute the three-dimensional panel deflections and in-plane strains based on images obtained from a calibrated pair of cameras focused on the back side of each panel. The panels were painted with 0.625-in.-diameter black dots, on 1-in. centers, on a white background. For the 20-ply panel a pair of Photron model SA5 cameras (Photron USA, San Diego, CA) were mounted on a tripod behind the panel in such a way that the whole panel was visible. These cameras had a resolution of 832 pixels along the length of the panel and 600 pixels across the width, a frame rate of 15000 frames/s and an aperture time of 1/59000 s. For the 24-ply panel, a pair of Photron model SA1.1 cameras was used, in a similar configuration. The camera resolution along the length of the panel was 704 pixels and 448 pixels across the width. The frame rate was 18000 frames/s and the aperture time was 1/49000 s. The system used on the 24-ply panel is shown in Figure 22.

To measure the kinematics of the blade impacting the 20-ply panel, the commercial software PONTOS (GOM mbH, Germany) was used in conjunction with a pair of Phantom V7.3 cameras (Vision Research Inc.). The camera pair was mounted forward and to the right of the engine axis viewing the area from the blade release to the panel impact. These cameras had a frame rate of 12500 frames/s, a horizontal resolution of 768 pixels, a vertical resolution of 504 pixels, and an exposure time of 20 μs. Figure 23 shows the camera pair location relative to the test hardware and Figure 24 shows a representative frame from the video after blade release and prior to impact. The white dots on the blade and the test article were individually tracked in order to obtain blade linear and angular velocity during the test. However, because of the large amount of light generated from the explosive charges used to release the fan blades and the resulting overexposure of the images, only a portion of the free flight of the blade segment could be tracked.

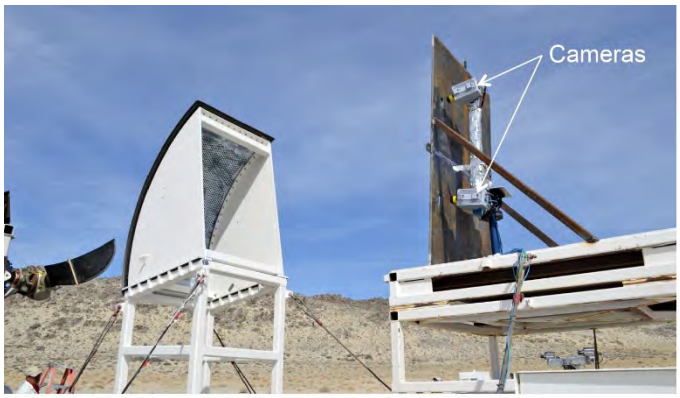

Figure 22.—Photogrammetry camera setup for 24-ply panel.

Figure 23.—Cameras used to measure blade kinematics.

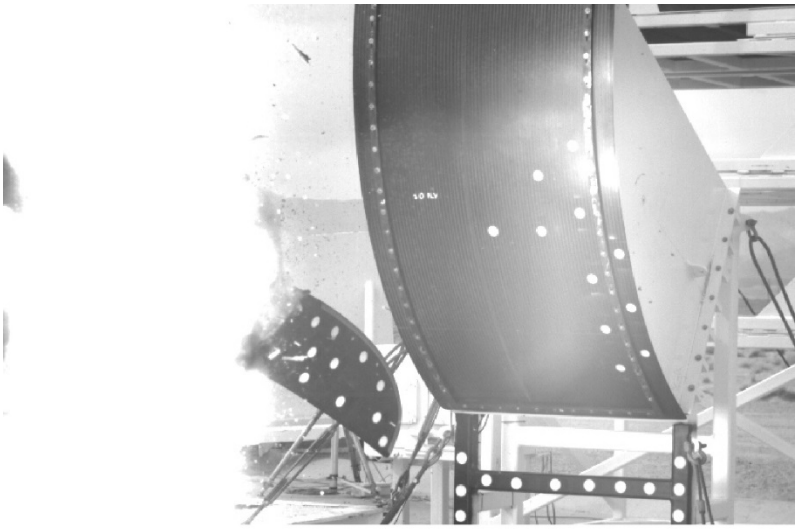

Figure 24.—Still image from one video camera used to track blade.

3.6 Blade Release

A linear shape charge was placed at the separation point of the blade. The shape charge was affixed to the fan blade by an adhesive and covered with a thin fiberglass strip, as described in Section 3.7.2. The fiberglass strip was used to ensure that the shape charge remained in the correct position even when the blades are at maximum velocity, while minimally impacting airflow.

3.6.1 Blade Release Firing System

Based on the analysis performed by NASA Glenn, the ideal release angle for the blades was predicted to be between 0° and 13° past vertical blade position. The WSL has developed a blade release firing system to provide precise release of the blades. This blade release firing system is designed to release the blades within ±1° of the ideal release angle.

The firing system for this test event had to provide a high-voltage current pulse to four exploding-wire detonators, which initiated the linear shape charges that severed the blades. The firing pulse was timed to release the blades at the designated angle. This firing system had to meet the safety requirements defined in the WSL Standard Operating Procedures for Explosive Bridgewire Operations (EBW) requirements. A graphical representation of the firing system is shown in Figure 25.

The blade position was detected by using a Banner Engineering Corp. model PD49 retroreflective laser sensor. This provided a blade "zero time" pulse to a timing box. A variable potentiometer in the timing box allowed manual adjustment of the delay from blade "zero" to a targeting camera strobe pulse and to a fire pulse logic circuit. The targeting camera was aligned with the desired firing position.

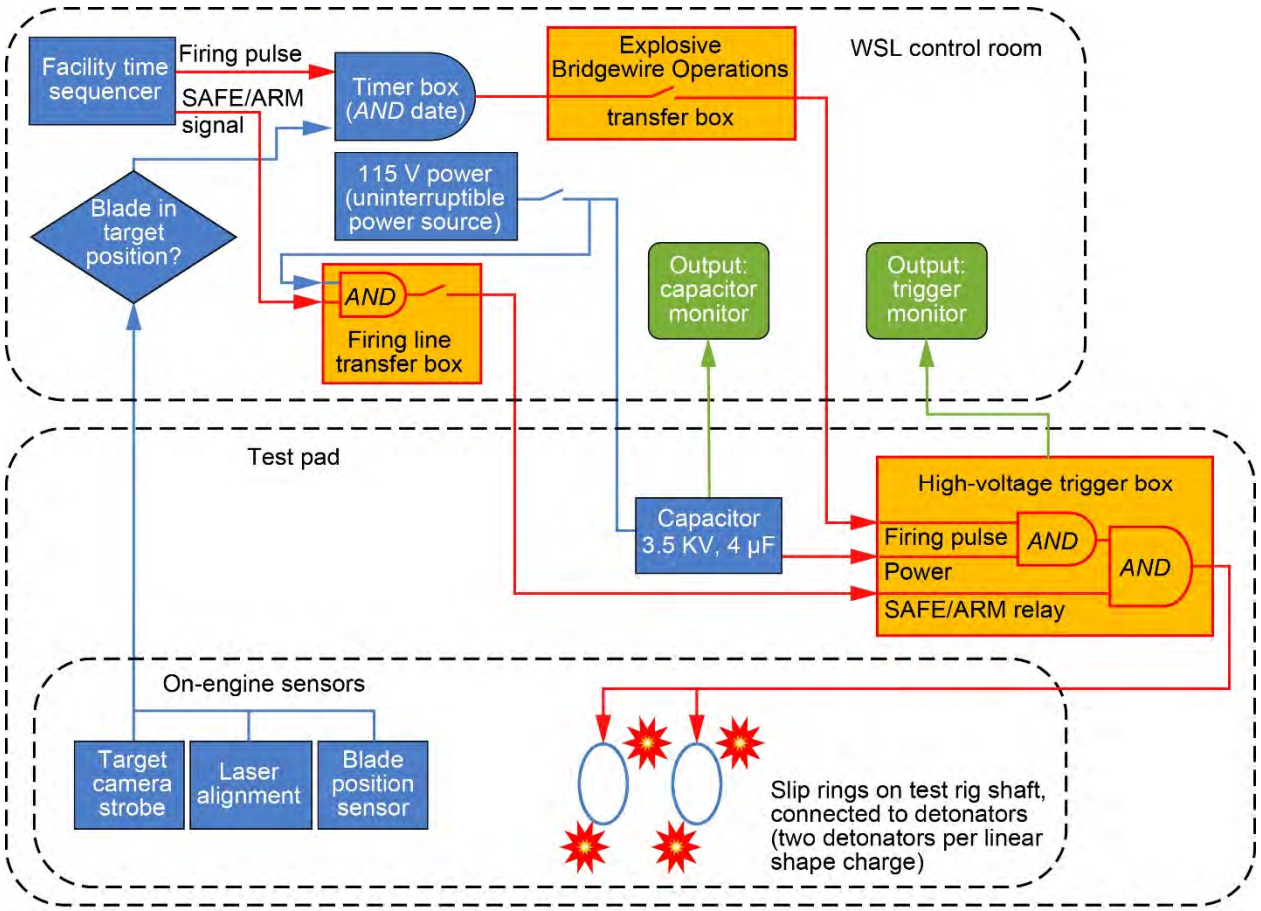

Figure 25.—Weapons Survivability Lab (WSL) blade bridgewire firing system.

The timing pulse was set by adjusting the potentiometer so that the target blade was correctly aligned within the camera view. The logic circuit would not pass the firing pulse until the facility sequencer provided the firing pulse. A targeting laser provided a visual aid for fine adjustment. When all conditions for a test were met, the facility time sequencer was started. When the time sequencer countdown reached zero, the fire pulse was allowed to propagate to the test pad electronics.

Two electronic boxes sat on the pad. The high-voltage box provided 3000 to 3500 V. The high-voltage trigger box provided the electronic switch to control the high-voltage power supply. To reduce the vulnerability of the high-voltage trigger box electrical noise, optical isolators were used. Also, to prevent the system from firing if de-energized, uninterruptible power supplies were used for each element of the firing system. Additionally, a Safe/Arm relay was installed to interrupt the fire pulse at the isolation transformer until sequencer time zero, which will only allow the switch to function during the first revolution. Monitoring circuits were also installed to detect any problems in the test environment.

The high voltage traveled through slip rings mounted on the propeller shaft to the exploding-wire detonators on the propellers. Multiple tests were conducted to test the firing system prior to the full-up blade release testing. The firing system functioned nominally during this test.

3.6.2 Linear Shape Charge Installation

Placement of the shape charge is indicated in Figure 26. Exploding-wire detonators were placed on either end of each linear shape charge. The two detonators provided redundancy, allowing the full length of the explosive to fire if any single wire had broken or if there had been a discontinuity in the linear shape charge.

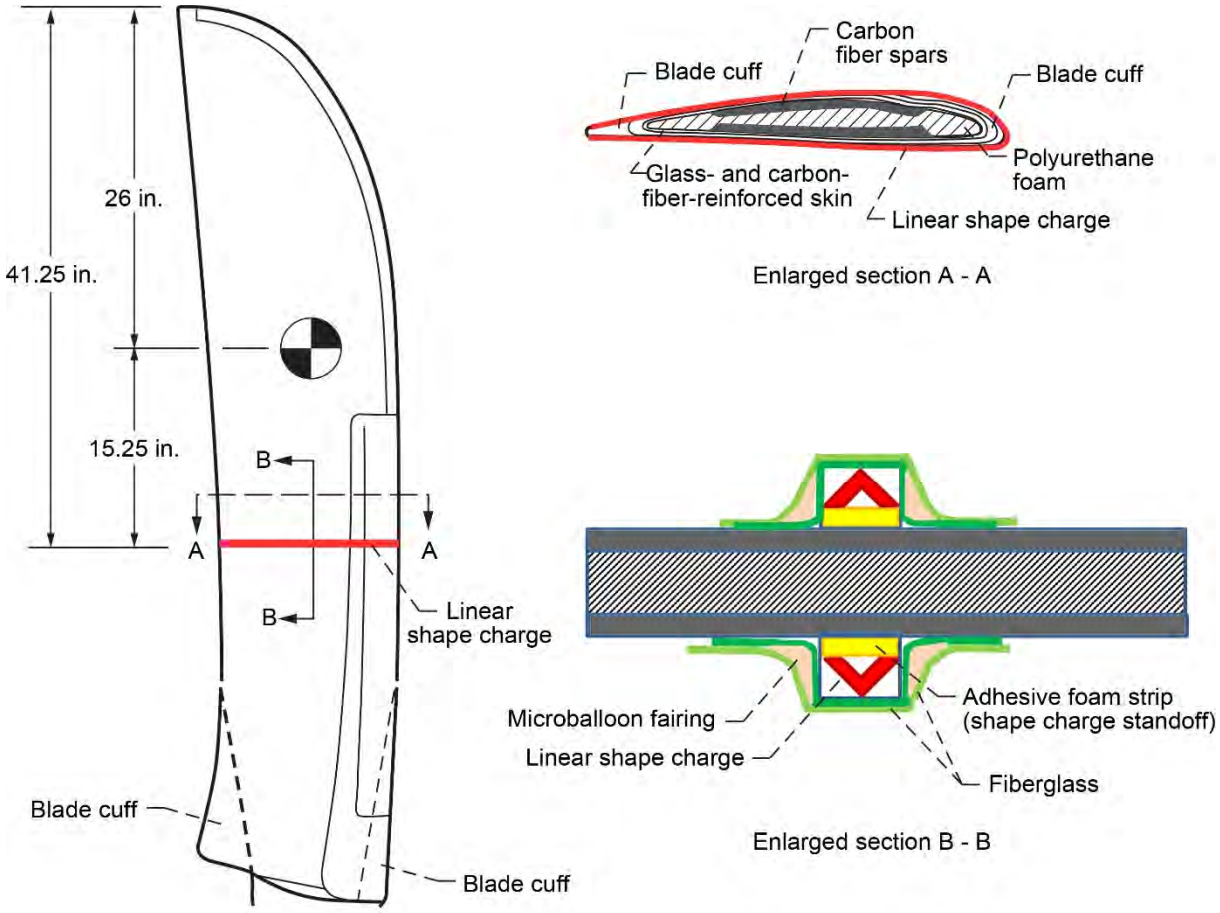

Figure 26.—Shape charge installation and released blade dimensions.

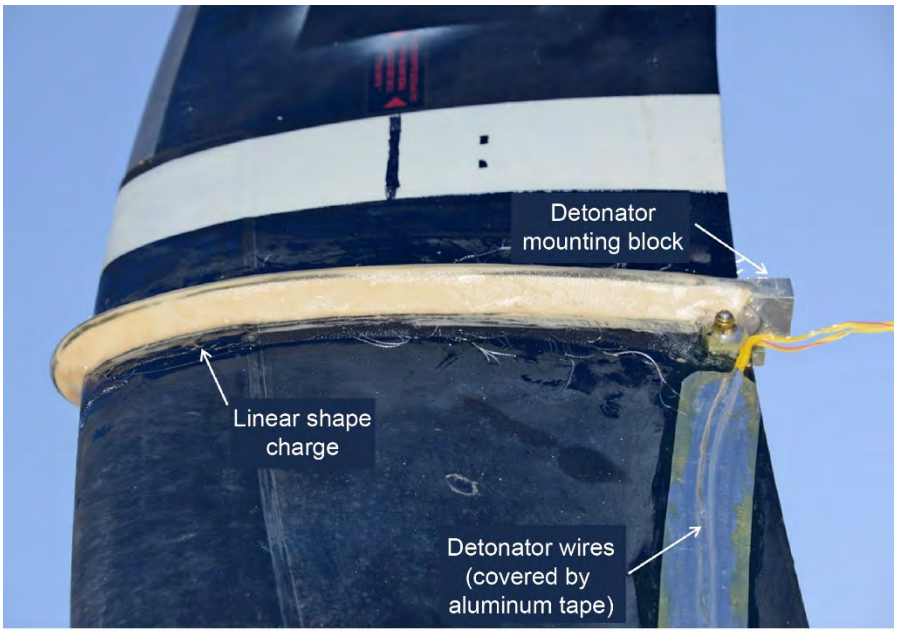

Figure 27.—Linear shape charge final installation.

The linear shape charge has a foam adhesive strip to provide the proper standoff distance to the material to be cut. To attach the shape charge more securely to the blade, a layer of fiberglass was placed over the shape charge. Additionally, microballoon filler was used to provide support, and a second layer of fiberglass was applied (Figs. 26 and 27).

4.0 Pretest Prediction(s)

Pretest predictions were based on the analysis conducted by NASA Glenn Research Center, documented in Reference 1. Based on the analysis, the fan blade was not expected to penetrate the 24-ply (0.52-in.) composite panel, but was expected to fully penetrate the 20-ply composite panel.

5.0 Test Results

Testing was conducted on February 20, 2014. All facility systems functioned nominally, and the blades were released as intended, at 8° past vertical (Fig. 28). The test conditions are noted in Table IV. The blades separated as intended and struck the composite test panels.

Figure 28 shows a composite photograph of the release of the blades just before shape-charge detonation, just after the shape charges were fired, and at first impact of the blades against the composite panels. The upper blade impacted the 24-ply panel and resulted in cracks, but no penetration. The lower blade impacted the 20-ply panel and, as predicted, penetrated the panel. The test results showed good correlation to the NASA analysis.

Data collected from the high-speed cameras were analyzed by NASA. The results of the DIC analysis are presented in Section 5.3, Photogrammetry.

Additional analysis was conducted to estimate the test impact condition. Blade-release velocity was analyzed by reviewing high-speed video and calculating velocity from engine revolutions per minute. Geometry of the test and timing from the high-speed video provided a calculated blade fragment velocity of 534 ft/s. A second calculation was conducted based on propeller speed (revolutions per minute) and an estimated blade fragment CG radius of 54.5 in. This calculation resulted in a blade velocity of 533 ft/s.

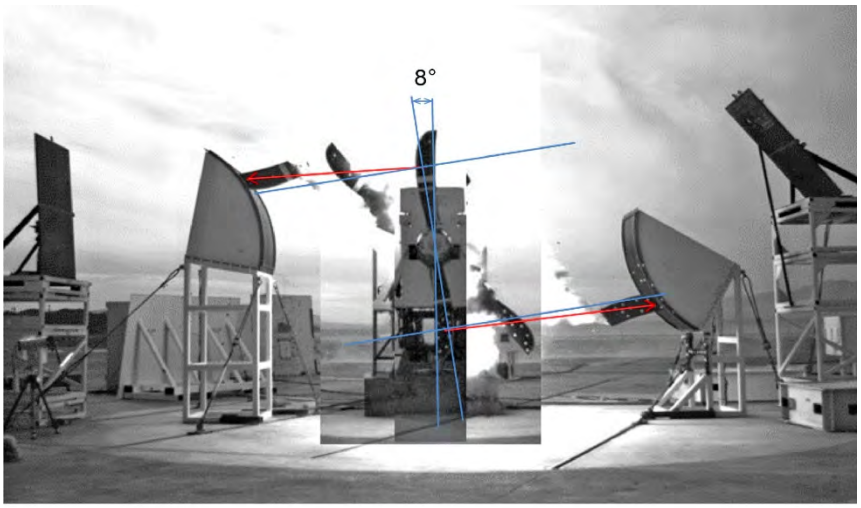

Figure 28.—Blade release with release angles.

TABLE IV.—TEST CONDITIONS

Test condition	Desired (24-ply/20-ply panel)	Actual (24-ply/20-ply panel)
Blade release position, deg	188/8	188/8
Blade velocity, rpm	1108	1120
Blade release velocity, ft/s	527	533
Blade weight, lb	15.1	
Distance of blade impact (forward of plane of rotation), in.	5	12.5/11.5
Blade kinetic energy, ft-lb	68 657.41	67 188.32
20-ply panel thickness, in.		0.452
24-ply panel thickness, in.		0.560

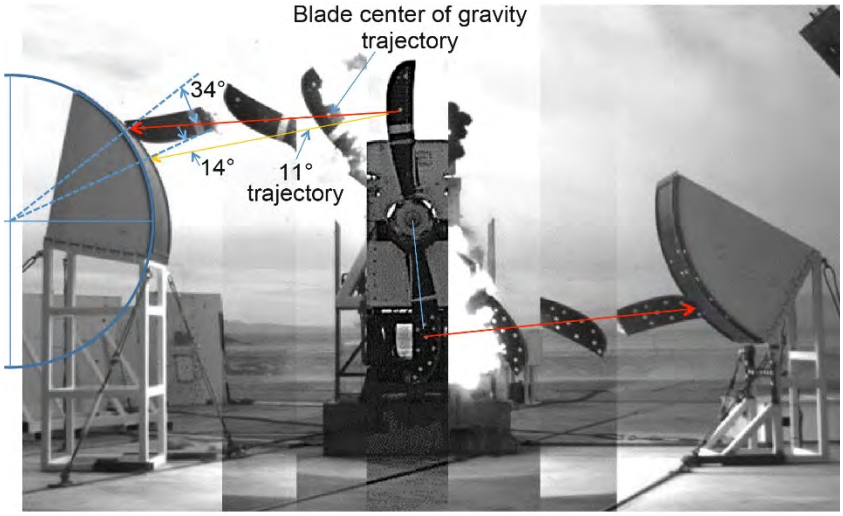

Figure 29.—Blade release with trajectory and obliquity.

Blade fragment trajectory was also estimated by reviewing high-speed video. The blade segments were released at 8° and 188° from vertical. From video analysis, the blade fragments traveled on a trajectory 4° less than the 8° and 188° perpendicular paths, resulting in the blade fragments impacting the panels above and below, respectively, the intended impact point. The blade trajectory obliquity was also calculated from video images. Figure 29 shows the impact obliquity for the upper-release blade is estimated to be 34°. Also shown is the obliquity of 14° that is predicted for an 11° release angle.

5.1 Lower (20-Ply) Composite Panel Test Results

The release angle of the lower blade was 188°. The blade released cleanly from the hub and rotated about the CG of the released fragment. The trajectory of the blade was approximately 4° above horizontal. The blade impacted tip first, with the length of the blade along the velocity vector. The blade caused a large tear in the panel, approximately 45 in. vertically and 12 in. horizontally, and penetrated completely (Figs. 30 to 33). Two additional horizontal cracks, visible in Figure 30, caused delamination but did not penetrate the full thickness of the composite. After passing through the panel, the blade impacted the mount frame and deflected upwards from the test panel mounting fixture. Upon recovery of the blade on the test pad, the tip was missing and the residual length of the blade was only 36 in. (Fig. 34).

The back side of the panel had a matching crack vertically but had additional vertical and horizontal cracks along the bottom of the panel and up both sides of the panel that did not penetrate the full thickness of the panel (see Figs. 31 and 33).

The accelerometer block on the lower left side of the panel mounting fixture was dislodged and the P20–Y1 wire was cut during the impact and penetration of the blade through the material. Data from P20–Z2 spikes to 1500 g approximately 9 ms after apparent impact, possibly indicating that debris impacted the accelerometer. The sustained high-g data (1500 g) for P20–Y2 is indicative of possible damage to the sensor, which was installed in the same mounting block as P20–Z2.

Ultrasound nondestructive inspection (NDI) of the 20-ply composite panel, shown in Figure 35, indicates a large area of delamination. The signal transmission scale is shown with the figure. No transmission at all (indicating delamination) is shown as white. The red dots throughout the green background are noise and are not indicative of damage. The small white holes along the border of the scan are the bolt holes for mounting the panel to the test fixture. The large white area on the scan indicates a large area of delamination, which corresponds to the visible cracks in the composite panel. The small patches of signal transmission within the large delaminated area may indicate partial damage or “kissing disbands”; however, this could not be determined from the ultrasound NDI. A thin line just below the bottom attachment of the panel to the fixture may indicate damage due to the mounting structure. A thin white line protruding from the lower left area of the delaminated area was caused by a thin piece of material protruding from the crack, which blocked transmission of the signal, not a delamination.

The residual velocity of the blade after penetration of the panel was not determined because of the limited view of the back side of the composite panel. The tip of the blade was missing. The trailing edge was also damaged, but it is unknown at what point this damage occurred: upon impact with the panel or subsequent impacts with the lighting frame or the test pad. Material from the blade was wedged into the crack in the panel and was removed prior to NDI.

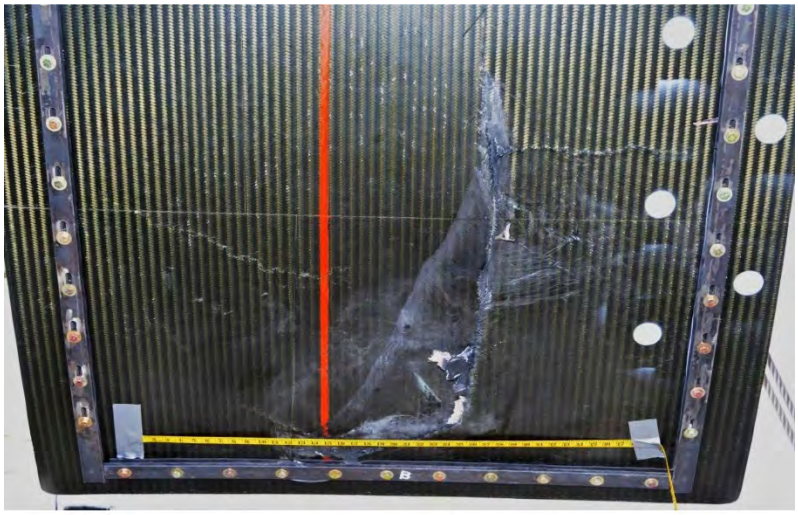

Figure 30.—20-ply composite panel postimpact damage, front side.

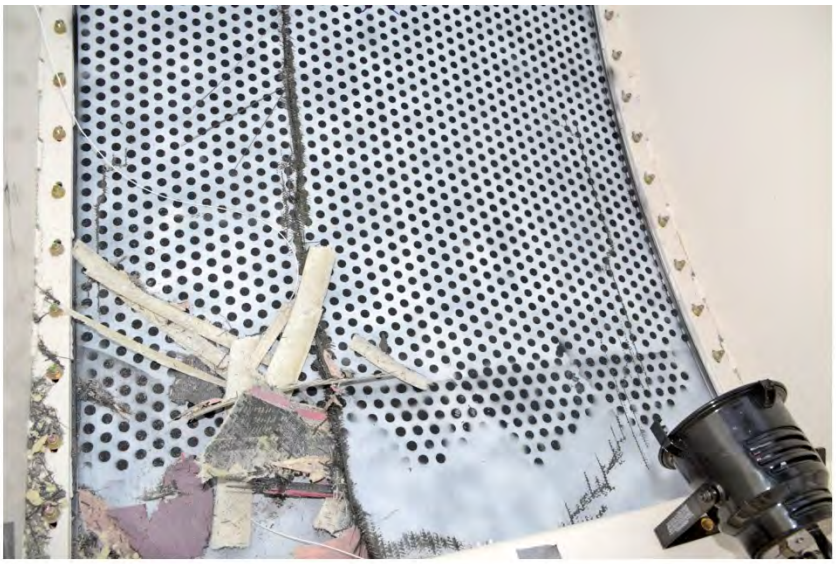

(a)

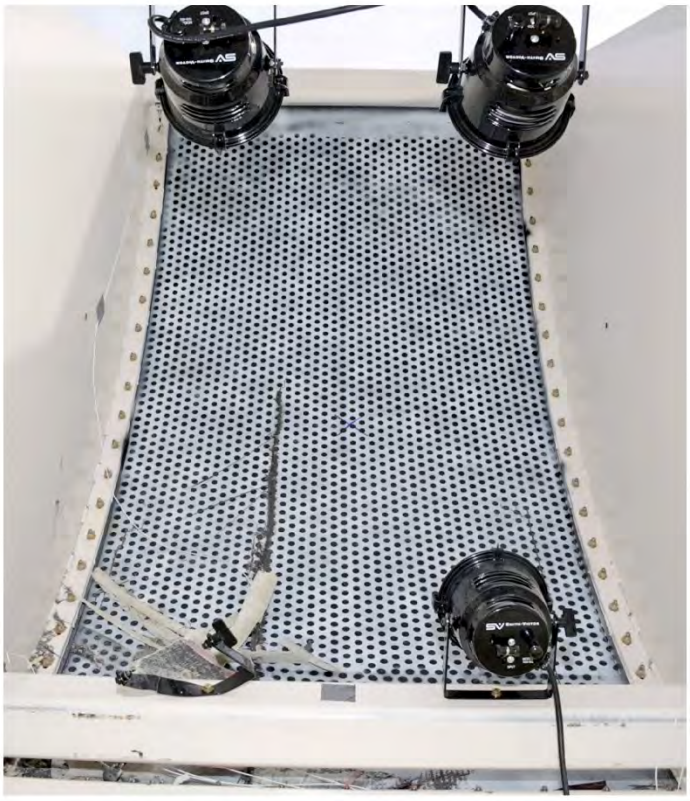

(b)

Figure 31.—20-ply composite panel, back side. (a) Lower right corner. (b) Full panel.

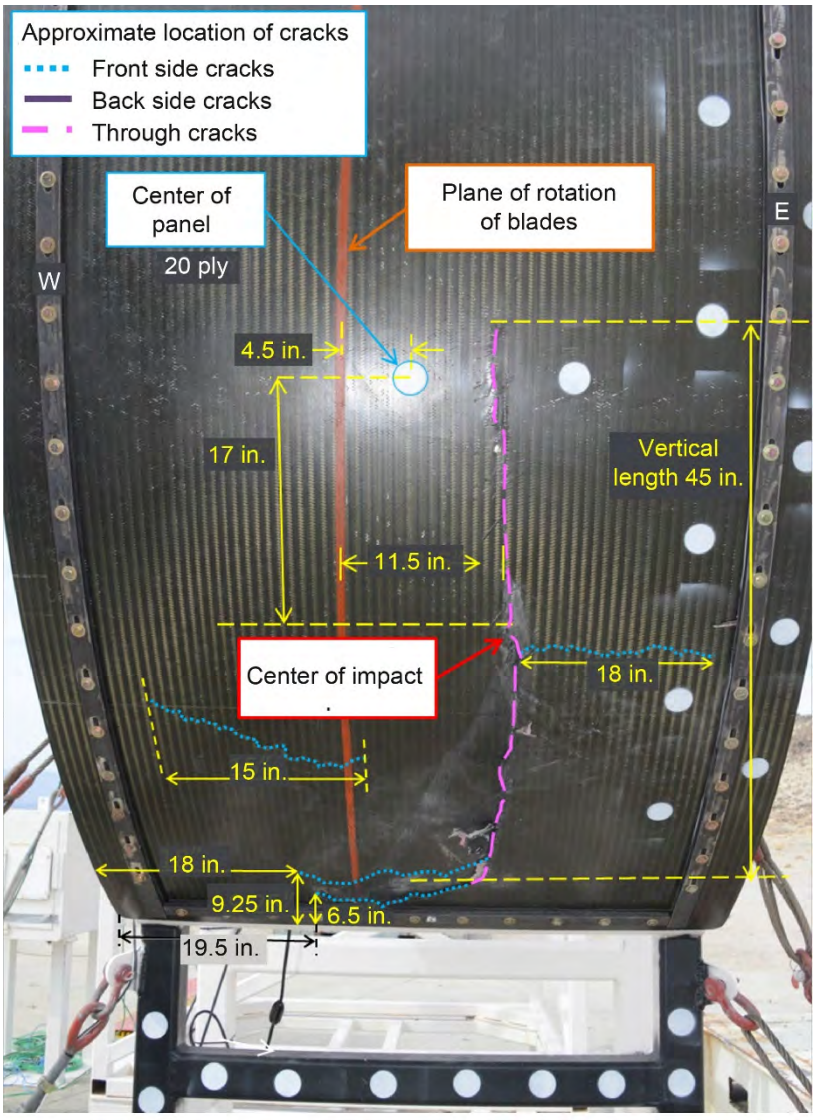

Figure 32.—20-ply composite panel postimpact damage, front side, with measurements.

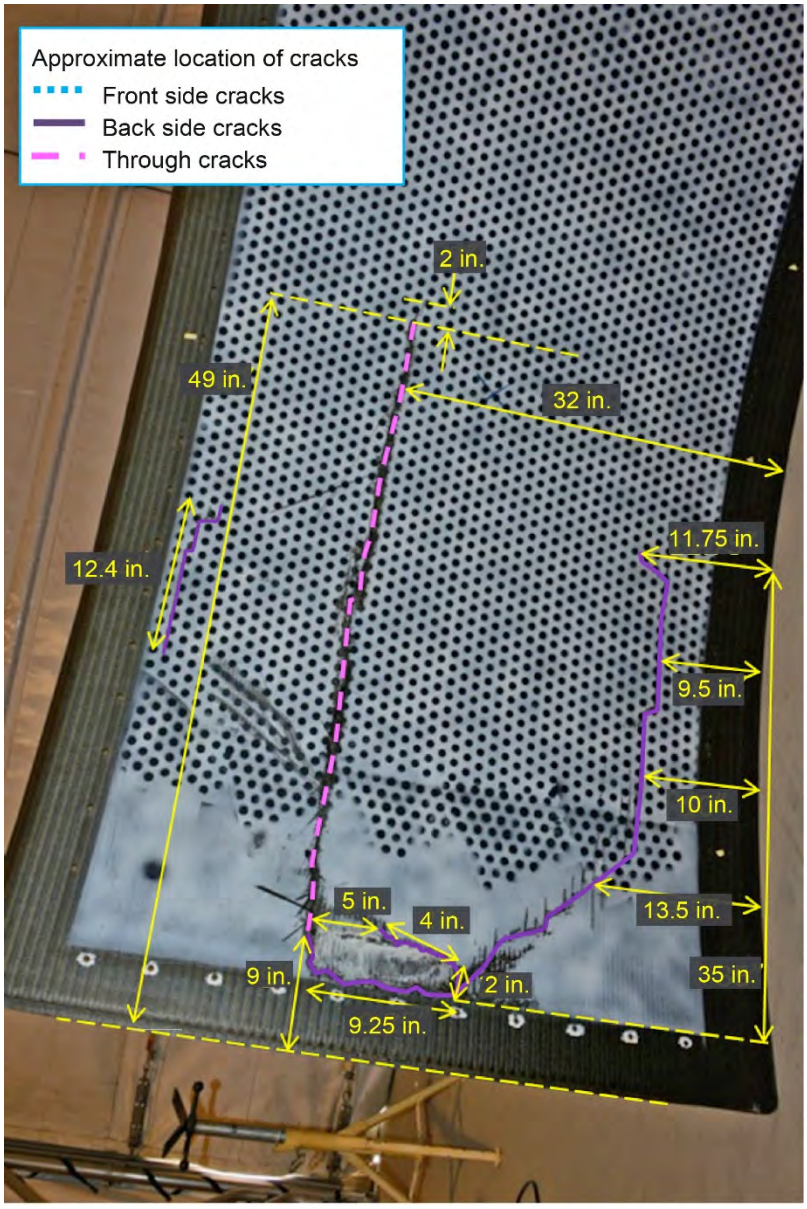

Figure 33.—20-ply composite panel postimpact damage, back side, with measurements.

Figure 34.—Lower blade after penetration of 20-ply composite panel.

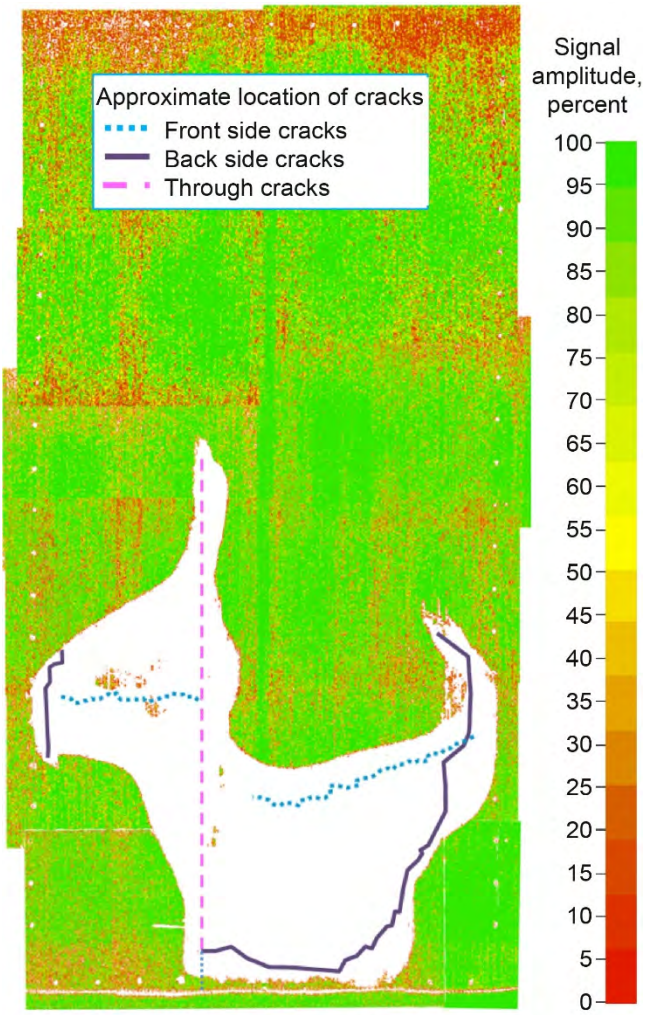

Figure 35.—Posttest ultrasonic nondestructive inspection of 20-ply composite panel, back side.

5.2 Upper (24-Ply) Composite Panel Test Results

The release angle of the upper blade was 8°. The blade released cleanly from the hub and rotated about the CG of the released fragment. The trajectory of the blade was approximately 4° below horizontal. The blade impacted tip first, with the length of the blade aligned with the velocity vector. The blade caused tears on both the front and back of the panel, but the tears were not aligned with one another and did not penetrate the panel completely. The damage to the composite panel is shown in Figures 36 to 39. Tears on the front side are visible in Figure 36, and tears on the back side are indicated by the arrows in Figure 37.

Figure 36.—24-ply composite panel postimpact damage, front side.

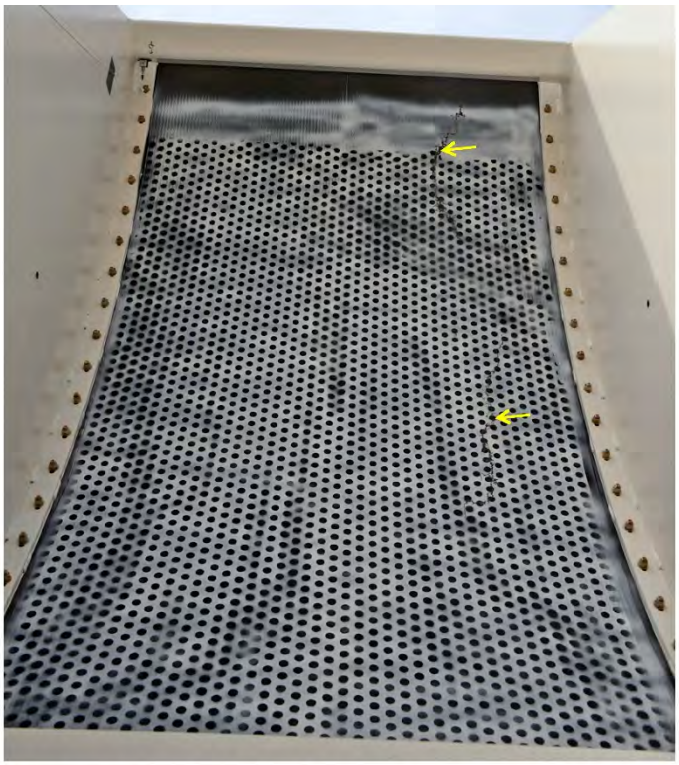

Figure 37.—24-ply composite panel postimpact damage, back side.

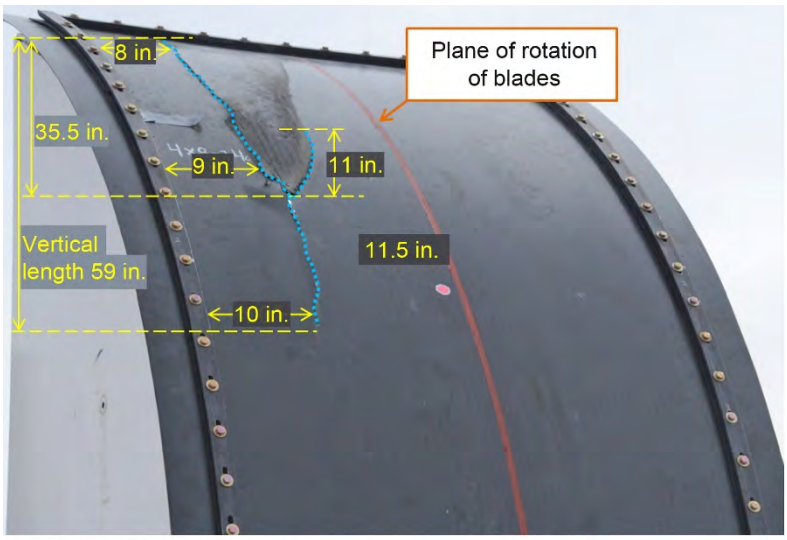

Figure 38.—24-ply composite panel, front side, with measurements.

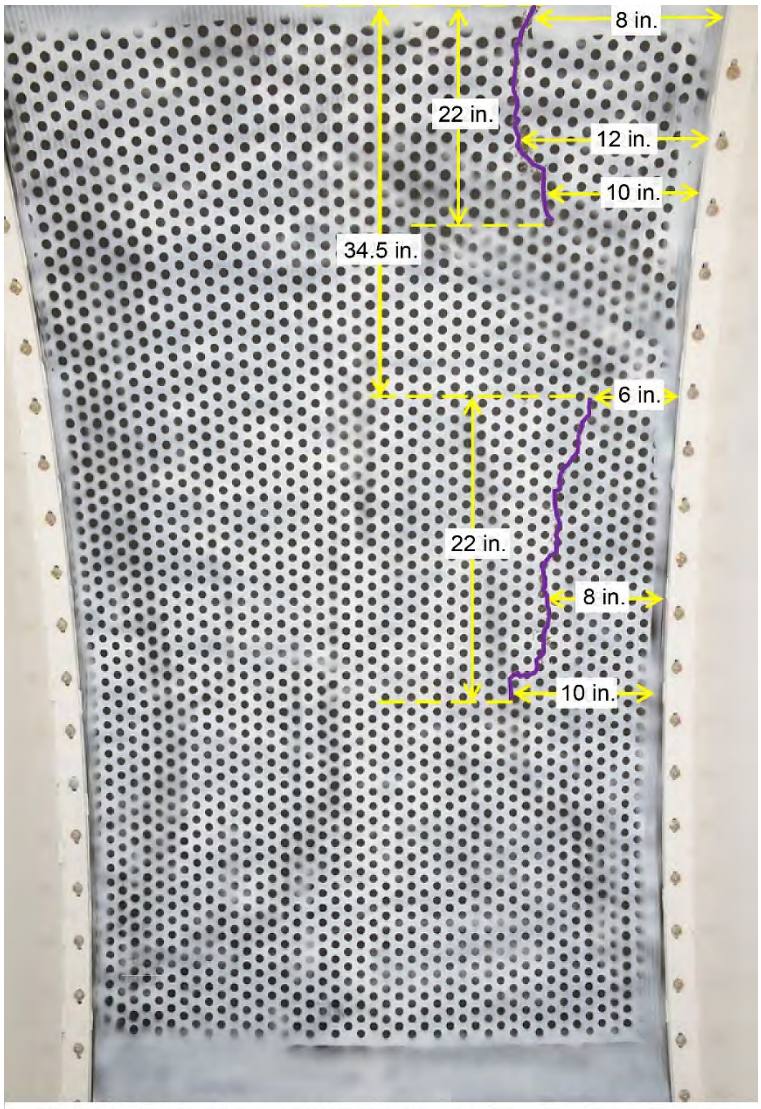

Figure 39.—24-ply composite panel, back side, with measurements.

The blade deflected upwards after impact and landed on the test pad. The tip and leading edge of the blade were crushed on impact, and the remaining tip and leading edge had no residual strength (Fig. 40). The residual length of the blade was 41 in. and weighed 11.2 lb.

Figure 41 shows the results of the NDI scan of the 24-ply panel. No transmission at all (indicating delamination) is shown as white. The red dots throughout the green background are noise and are not indicative of damage. The small white holes along the border of the scan are the bolt holes for mounting the panel to the test fixture. The large white area on the scan indicates a large area of delamination, which corresponds to the visible cracks in the composite panel.

Figure 40.—Upper blade after impact on 24-ply composite panel.

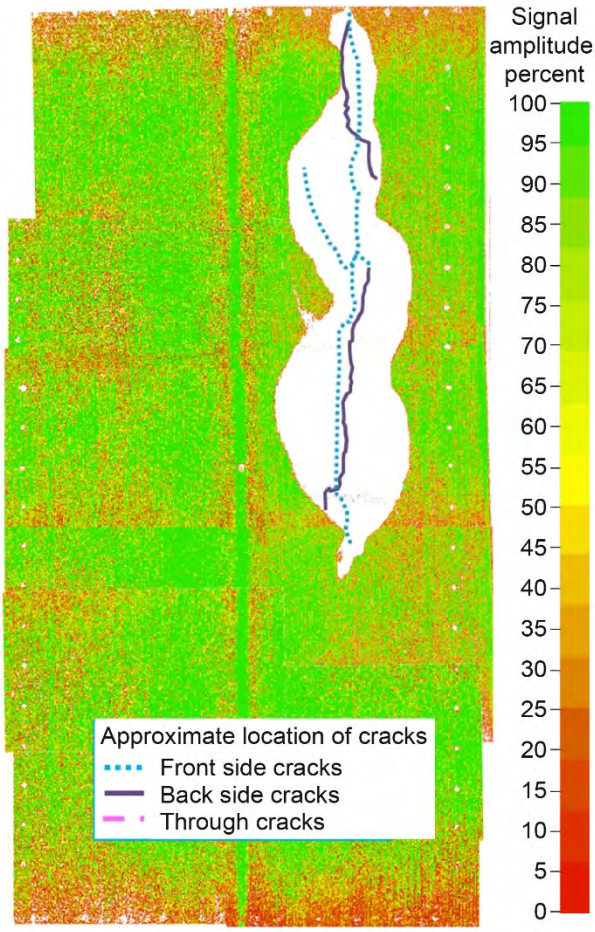

Figure 41.—Posttest ultrasonic nondestructive inspection of 24-ply composite panel, back side.

5.3 Results: Photogrammetry

Calibrated pairs of high-speed cameras and commercial DIC software were used to obtain quantitative measurements of blade kinematics and also panel displacements and strains.

5.3.1 Blade Kinematics

Photogrammetric measurements of the blade kinematics yielded the blade velocity, which impacted the 20-ply panel while in free flight. Figure 42 shows the resultant velocity as a function of time for the point estimated to be the blade CG (blue line) and a marker point near the blade tip (black line). There is some noise in the results, but the average resultant velocities over the measured time were 536 ft/s for the CG and 695 ft/s for the point near the tip.

5.3.2 Panel Displacements and Strains

Photogrammetric measurements of the back side of the 20- and 24-ply panels yielded measurements of the full-field displacements in three directions, and the resulting in-plane strains. For each test panel a local cylindrical coordinate system was established in which the origin was at the center of a cylinder that would be generated by extending the panel through 360°. Positive values of radial displacement are outward from the origin. With the given camera orientations, positive axial (y-direction) displacement is in the engine forward direction for the 20-ply panel and in the engine aft direction for the 24-ply panel. The results indicated that there was measurable deflection in the frame to which the panels were clamped. It was possible to measure the panel deflection relative to the frame by subtracting the average frame movement.

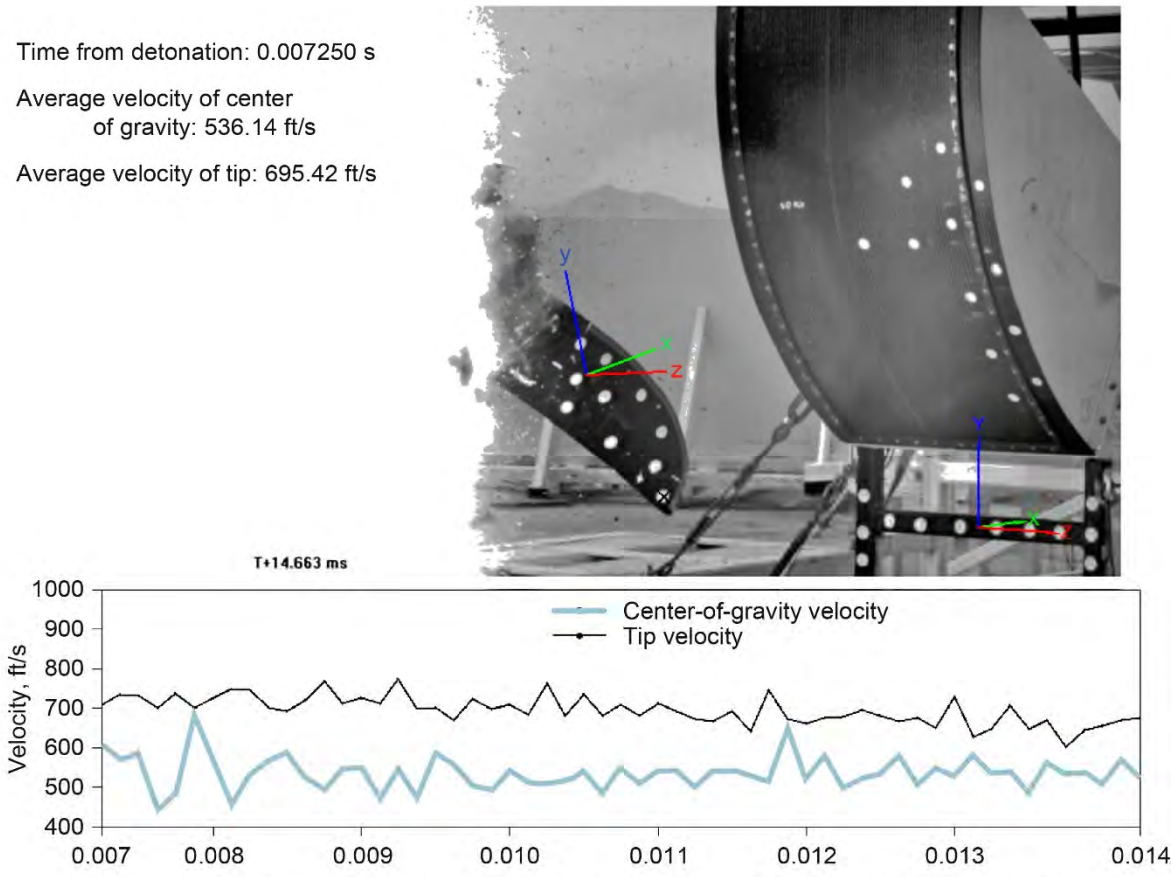

Figure 42.—Computed resultant velocity for two points on blade impacting 20-ply panel.

5.3.2.1 20-Ply Panel

The 20-ply panel was penetrated by the blade. At the point of maximum deflection prior to failure the radial displacement at the point of impact was 1.175 in. The radial displacements for the 20-ply panel are shown in Figure 43. Figure 43(a) shows a contour plot of the radial displacement just prior to failure, with positive values being inward in the general direction of blade travel. Figure 43(b) shows the deflection along the segment line shown in part (a) for a number of consecutive frames up to the point of failure.

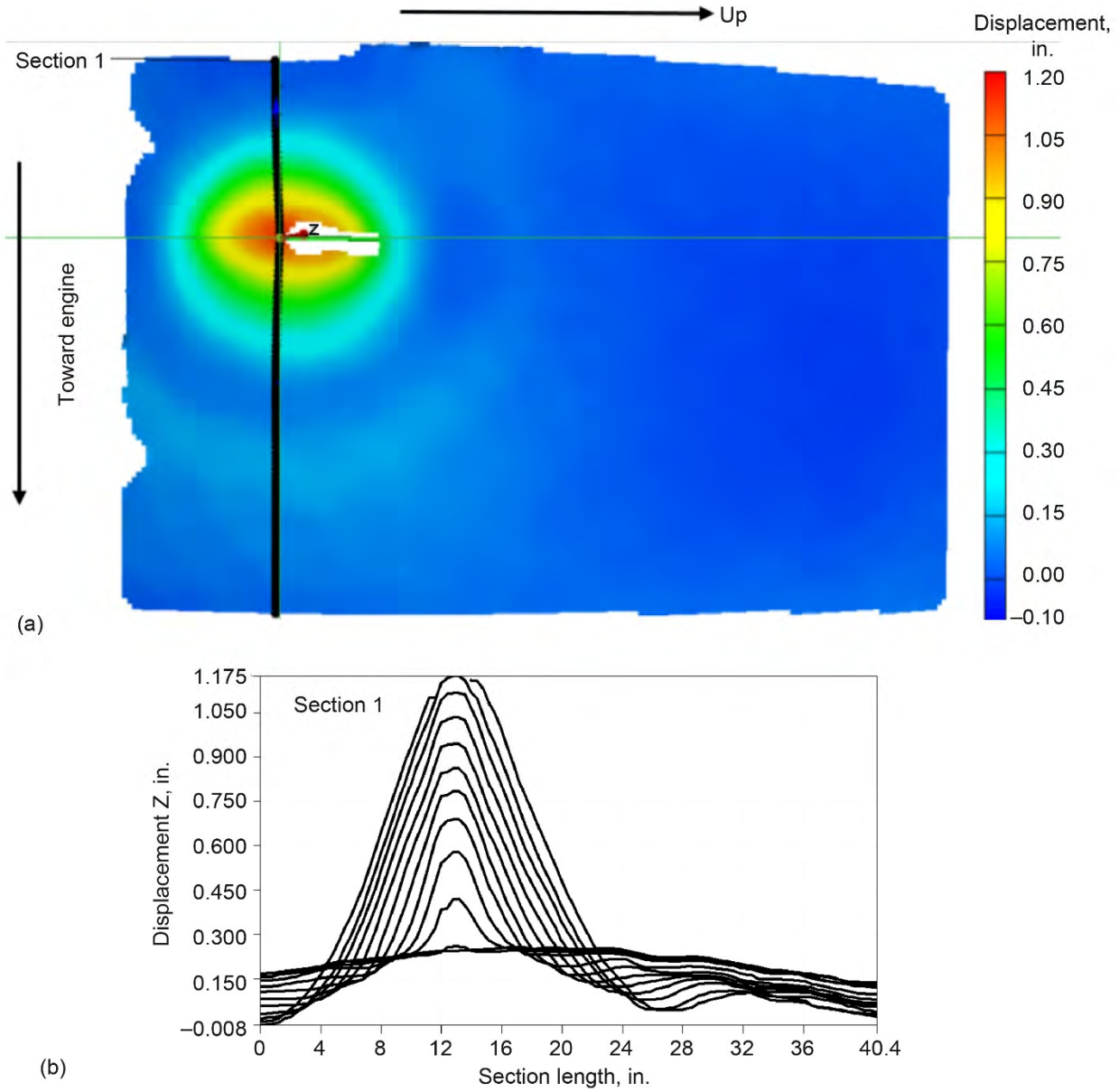

Figure 43.—Inward radial displacement of 20-ply panel after blade penetration. (a) Contour plot just prior to failure. (b) As function of length along segment line shown in part (a) for several frames up to time of maximum deflection; time between each line is 66.7 ms.

Maximum principal strains for the 20-ply panel are shown in Figure 44. Figure 44(a) shows the distribution of maximum principal strain in the panel just prior to failure. At the point shown in the figure, the value was just over 1 percent.

The time history of maximum principal strain of the point indicated in Figure 44(a) is shown as a function of time in part (b) up to the point of failure. In the figure, blade impact begins at 0.000 s. Prior to this time there is a strain response likely related to the blast generated from the shape charge, which travels faster than the blade. After penetration occurred, tracking the points was no longer possible.

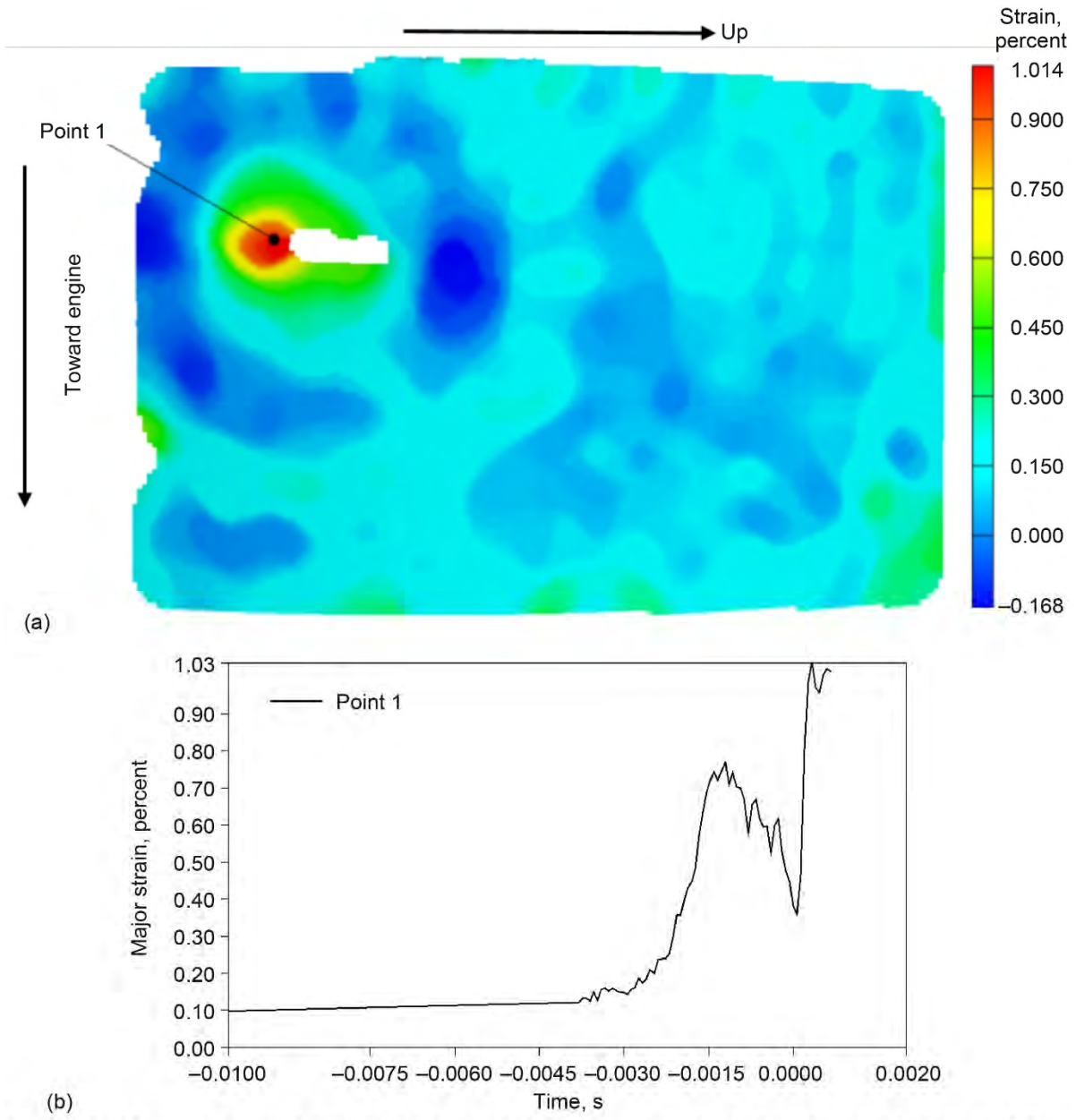

Figure 44.—Maximum principal strain in 20-ply panel after blade penetration. (a) Contour plot just prior to failure. (b) As function of time at point shown in part (a).

5.3.2.2 24-Ply Panel

The 24-ply panel was not penetrated by the blade, making it possible to measure displacements and strains at their maximum values.

5.3.2.2.1 Radial Displacements

The blade did not penetrate the 24-play panel, but cracks were generated both on the front and back sides of the panel. Two main cracks were generated on the back side as shown in Figure 39. Radial displacements for the 24-ply panel are shown in Figures 45 and 46. Figure 45(a) shows a contour plot of the radial displacement at the time of maximum panel deflection. This is the total displacement, including any contribution from the motion of the test fixture. A number of points are indicated in the figure. The points labeled “0” and “1” span the first crack that formed on the back side of the panel shown in Figure 39 between 2 and 2.5 ms after impact. A time history of the radial displacement of three of the indicated points is shown in Figure 45(b). Note that during the time of impact the displacement at point 2 is radially inward as would be expected, but the displacements at points 0 and 1 are outward indicating a highly dynamic process. The dashed vertical line in Figure 45(b) indicates the time at which the crack that formed between points 0 and 1 occurred. Figure 45(c) shows the radial displacement along the line labeled “Section 1” shown in Figure 45(a) for a number of consecutive frames up to the point of maximum deflection. Note that there is significant radial displacement at both ends of the segment line, which are near the fixture frame. This indicates that there is some motion in the frame itself. Although the motion of the frame is likely not a rigid-body motion, an attempt to measure the displacement of the panel relative to the frame was made by averaging the displacement of four points located at the corners of the measurable area and subtracting that motion from the overall deflection (Fig. 46). This measure of displacement relative to the frame is shown in Figure 46(a). Relative to the average of the four points, the maximum radial displacement is just over 2.6 in. This relative measure of radial displacement is shown as a function of time in Figure 46(b) for the seven points shown in part (a). There is a significant difference in the relative displacement shown in Figure 46(b) compared with the total displacement of the points shown in Figure 45(b).

5.3.2.2.2 Transverse Displacements

Displacements in the transverse (axial, y-) direction for the 24-ply panel are shown in Figures 47 and 48. Figure 47(a) shows the y-displacement (upward in the figure) in the panel at the time that the first crack initiated. The y-direction is in the engine aft direction. Two points labeled “0” and “1” that span the crack are shown in the figure. The y-displacement of these two points is shown in Figure 47(b) as a function of time. The dashed line in the figure indicates the time of initiation of this crack. The figure shows that initially the two points labeled “0” and “1” are moving together. At the point of crack initiation, indicated by the dashed line, the displacement of point 0 becomes greater than point 1 in the positive y-direction, indicating that the two points are moving closer together and that the crack that formed at this location is the result of transverse compressive strain. At this time this region of the panel is displacing in the positive (outward) radial direction.

Figure 48(a) shows the y-displacement of the panel near the time at which the second crack initiated near the panel boundary. This crack formed between the points labeled “7” and “8.” The figure shows that at this time there is generally an inward displacement of the panel near the upper and lower edges of the figure, possibly due to deformation of the frame fixture. The y-displacement of these two points is shown in Figure 48(b) as a function of time. In the figure, first impact occurs at 0.0000 s. The dashed line in the figure indicates the time of the initiation of the crack at this location. The figure shows that up until approximately 3 ms after impact, the y-displacement of the two points was essentially the same. After this, the displacement of point 8 was greater than that of point 7, indicating that the distance between the two points decreased. Right before failure, the relative displacement of the two points changed, and the distance between the two points began to increase, indicating that a tensile strain transverse to the crack location existed at the time of failure.

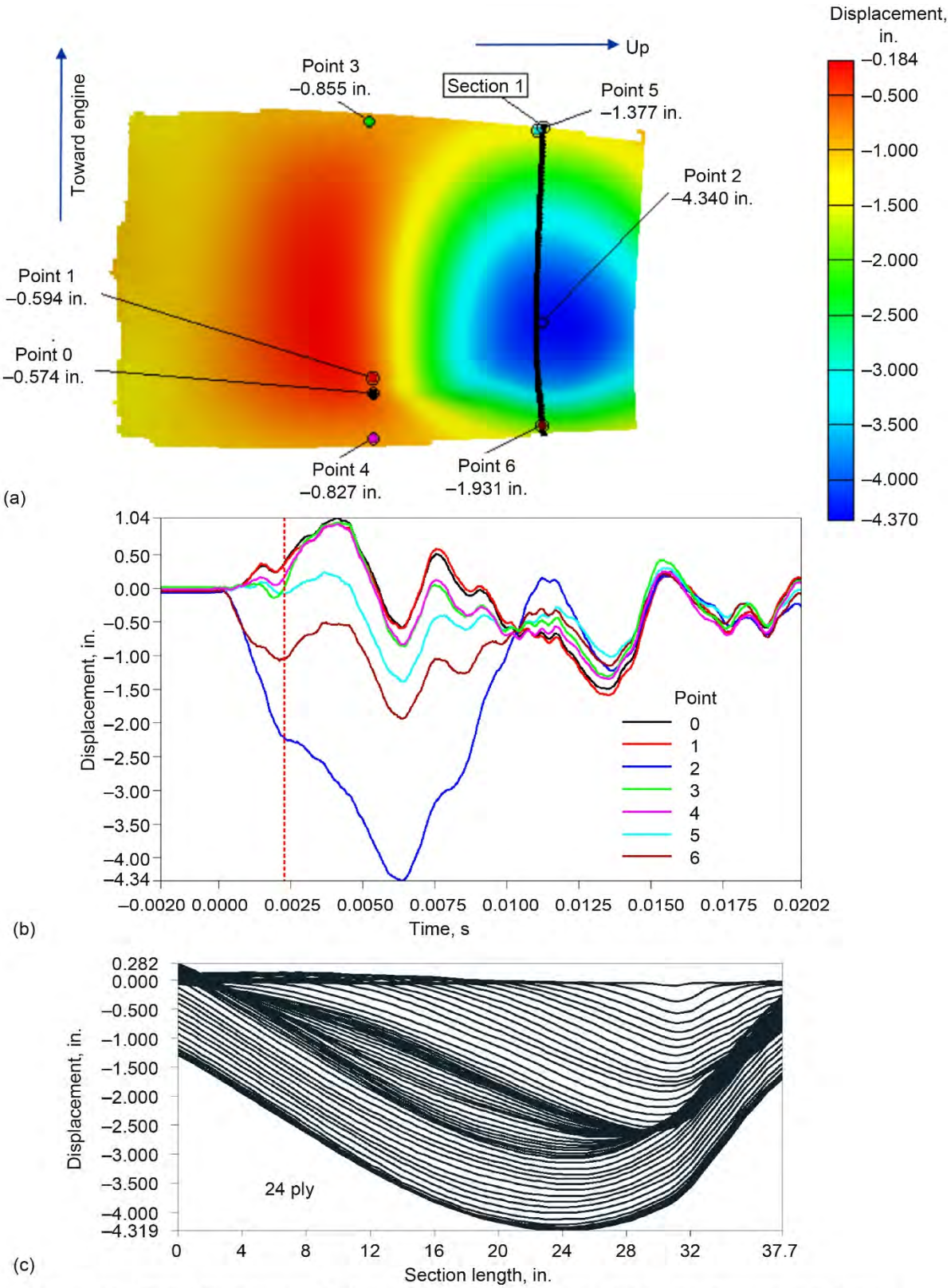

Figure 45.—Radial displacement of 24-ply panel during blade impact. (a) At time of maximum deflection. (b) As function of time for points labeled in part (a). (c) As function of length along Section 1 line shown in part (a) for several frames up to time of maximum deflection; time between each line is 111.1 μs.

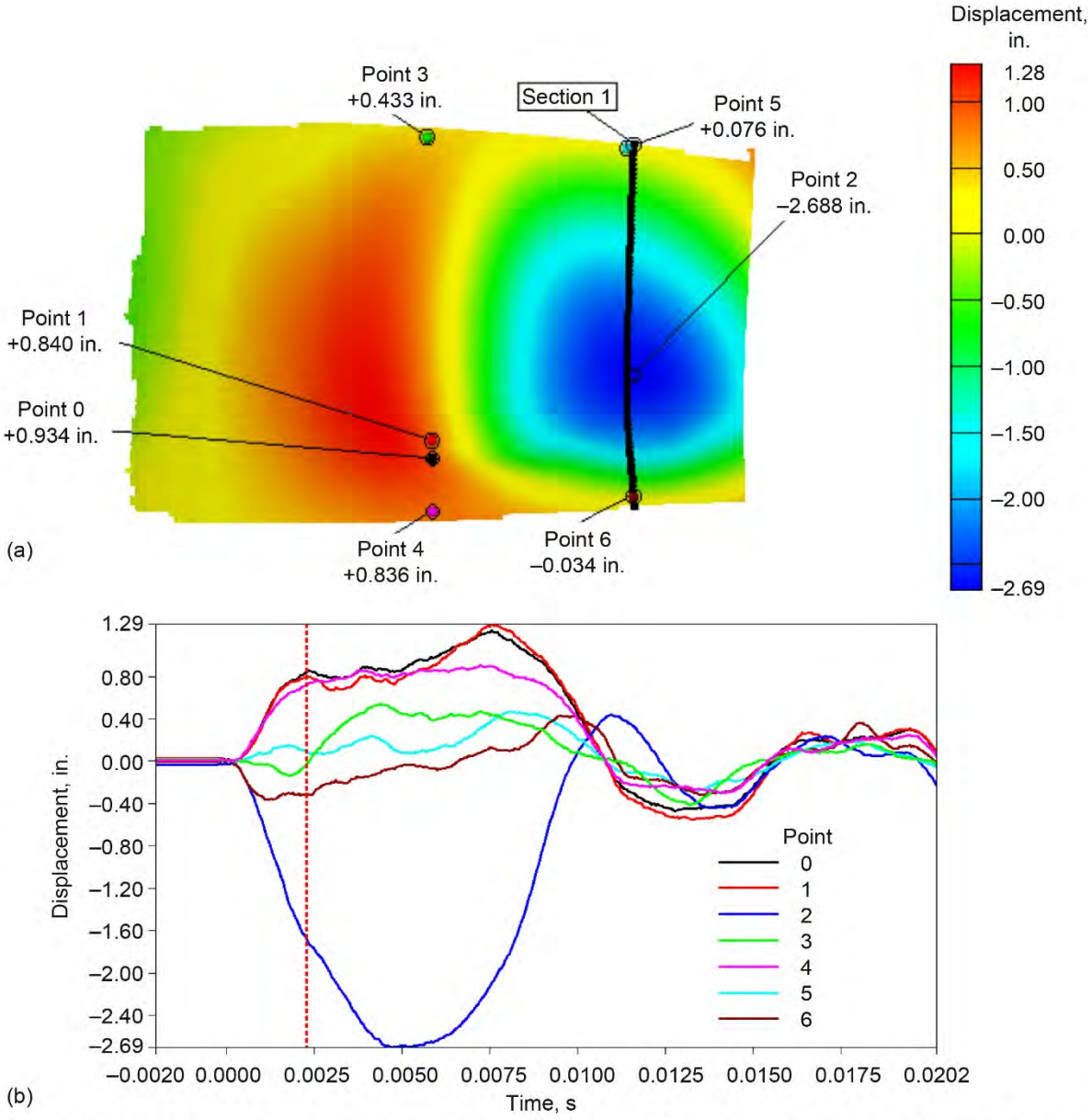

Figure 46.—Radial displacement of 24-ply panel during blade impact relative to average of four points at corners of measurable area. (a) At time of maximum deflection. (b) As function of time for points labeled in part (a).

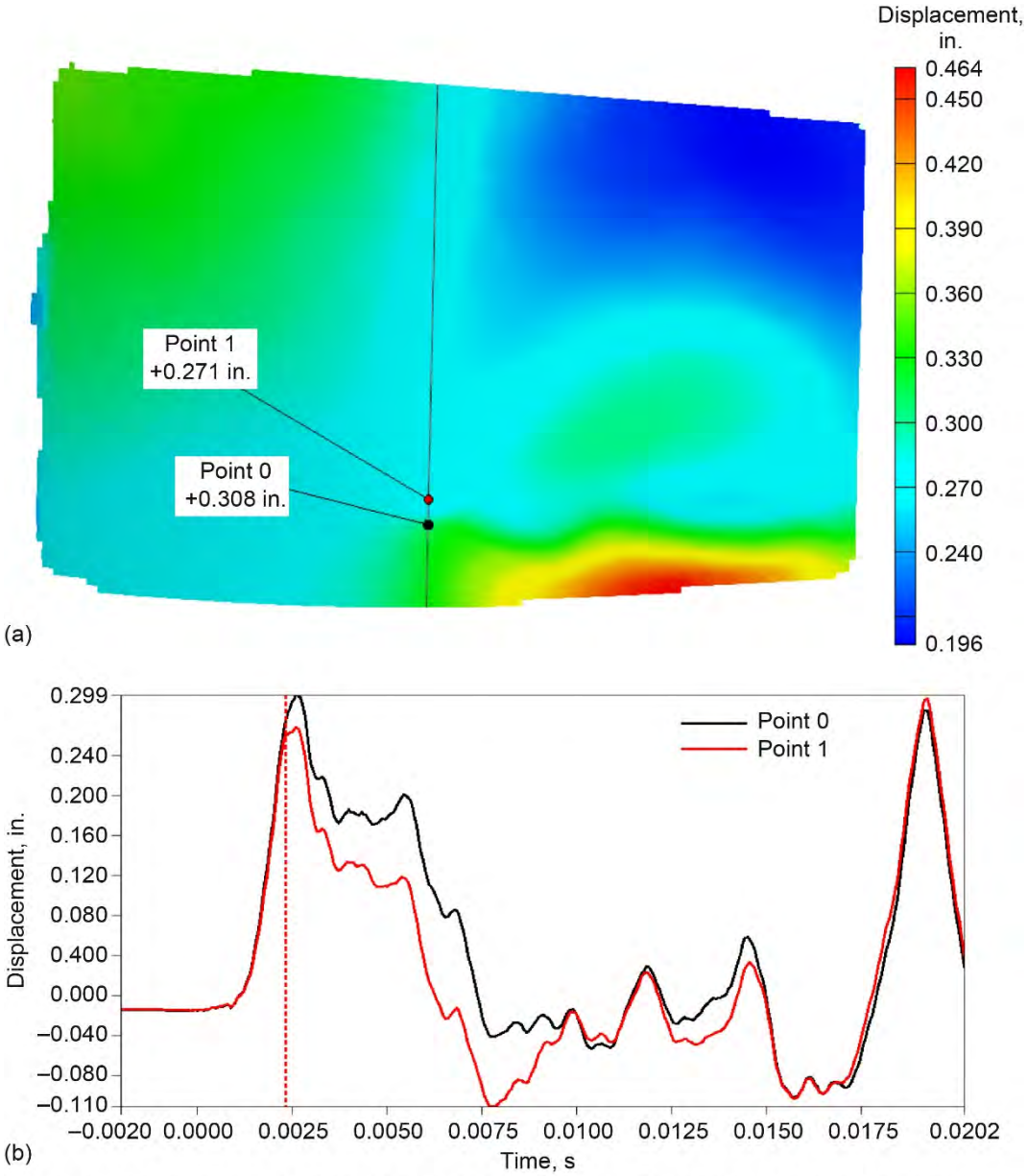

Figure 47.—y-displacement in 24-ply panel during blade impact. (a) At time first crack initiates. (b) Of points labeled in part (a) as function of time.

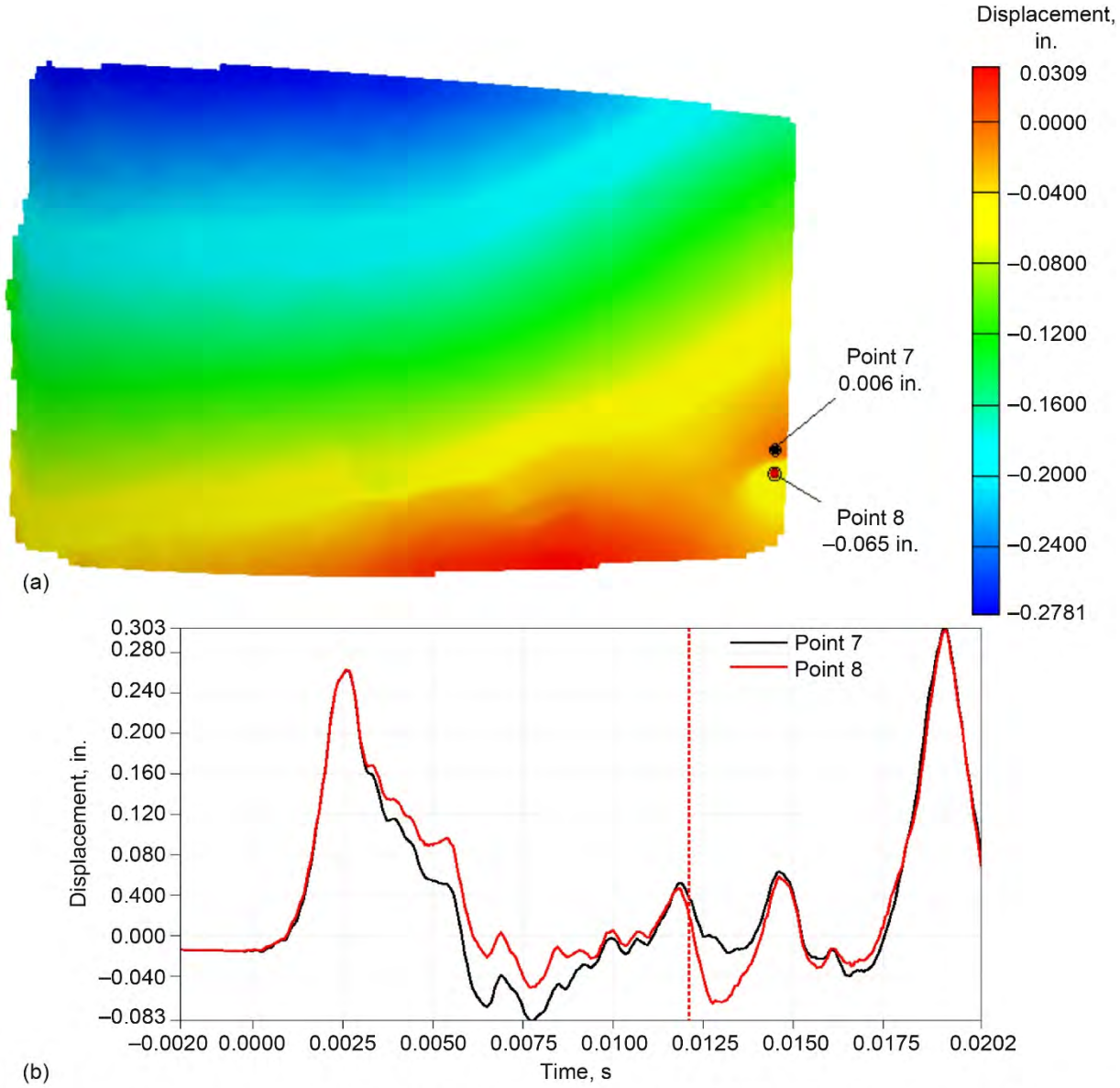

Figure 48.—y-displacement in 24-ply panel during blade impact. (a) At 0.0129 s, just after second crack initiates. (b) Of points labeled in part (a) as function of time.

5.3.2.2.3 Strains

Strains in the 24-ply panel are shown in Figures 49 to 51. The strain in the y-direction (transverse to the cracks) at the time of the first crack initiation in the 24-ply panel is shown in Figure 49(a). In the region of the formation of the first crack, between the points labeled “0” and “1,” the strain in the y-direction is compressive. The y-direction strain at these points is plotted as a function of time in Figure 49(b). Because of the limited resolution of the cameras, it was not possible to measure the strain at the exact location of crack initiation.

Figures 49(a) and (b) show that at the time of the first crack initiation this region was in a compressive strain state.

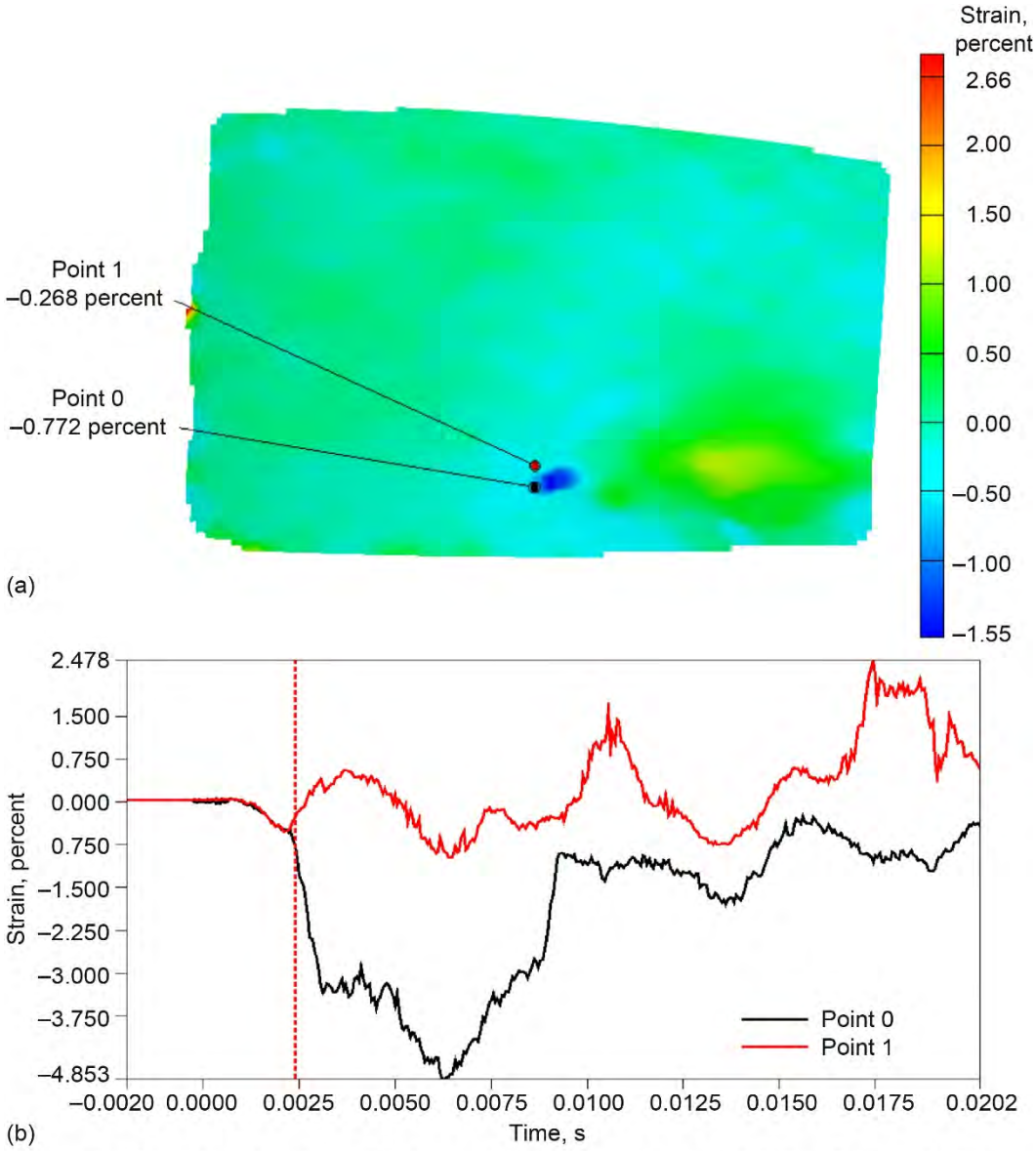

Figure 49.—Strain in y-direction in 24-ply panel during blade impact. (a) At time first crack initiates. (b) At points labeled in part (a) as function of time.

Figure 50(a) shows a contour plot of the strain in the y-direction (transverse to the panel cracks) at the time the second crack initiated. The second crack initiated at the panel boundary, which was outside of the computable area, so it was not possible to compute the strain at the initiation site. However, as seen in the figure, the transverse strain is generally positive in this region, indicating that the crack initiated as a result of tensile transverse strain. Figure 50(b) shows the strain in the y-direction for the two points indicated in part (a), as a function of time.

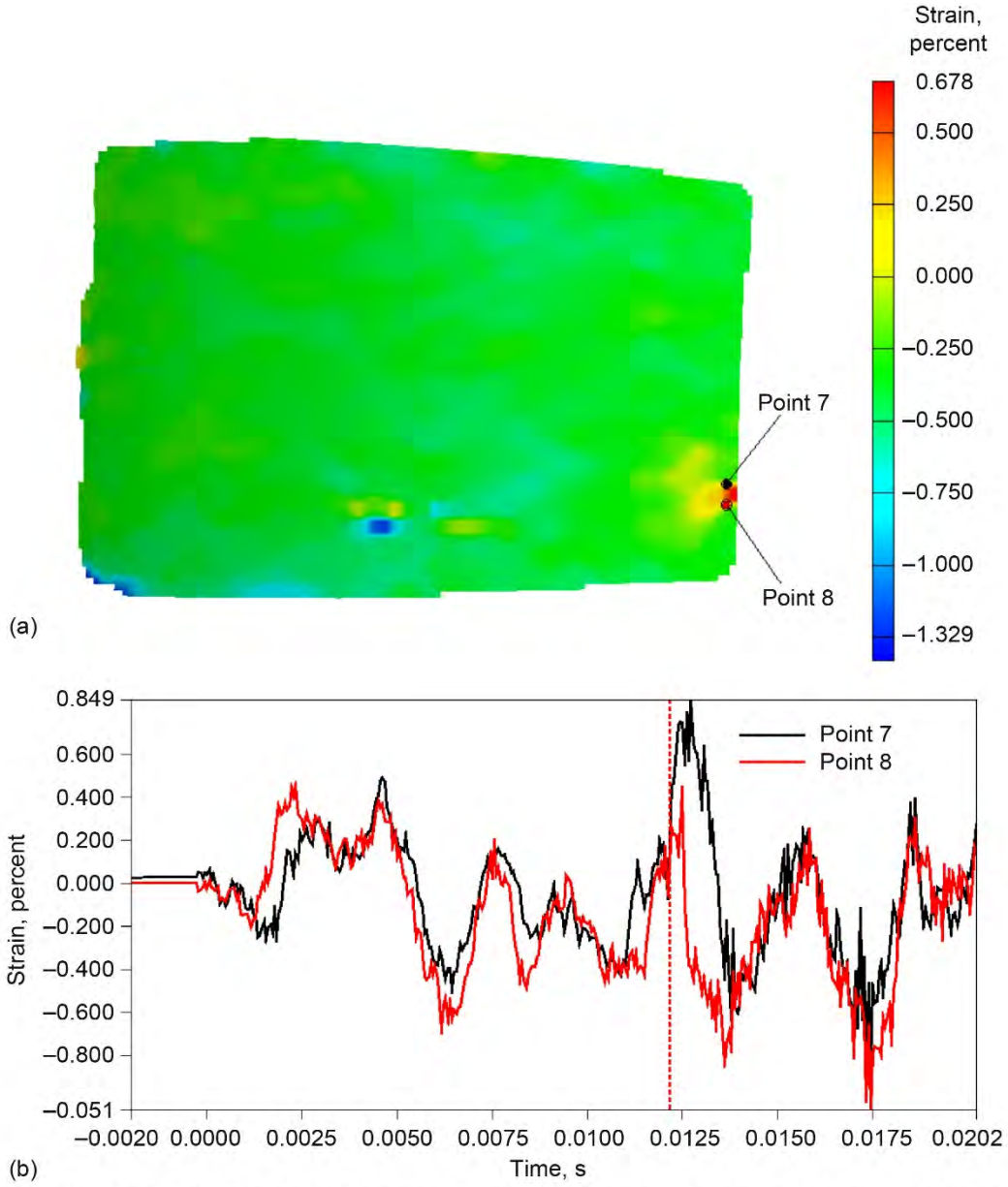

Figure 50.—Strain in y-direction in 24-ply panel during blade impact. (a) At time second crack initiates. (b) At points labeled in part (a) as function of time.

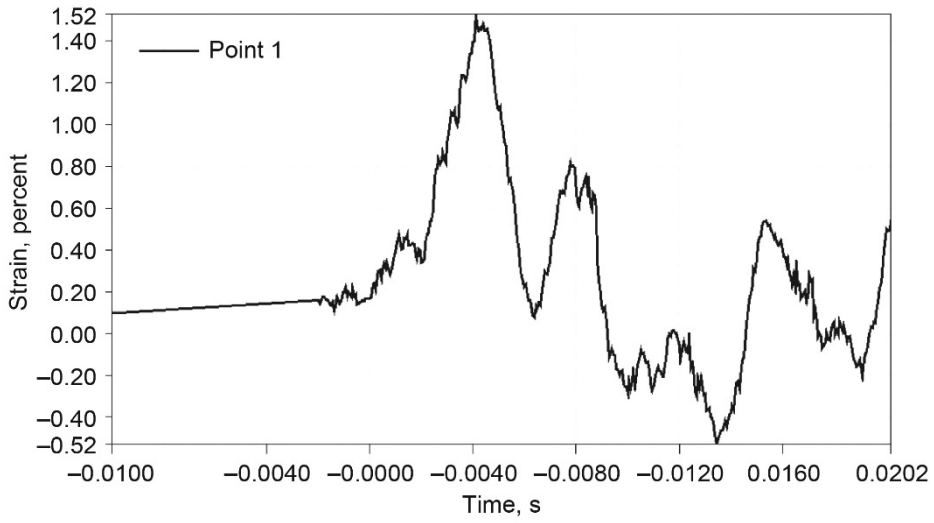

Figure 51.—Maximum principal strain at point of maximum deformation of 24-ply panel.

The maximum principal strain at the point of maximum deformation (indicated by point 2 in Figure 46(a)) is shown in Figure 51. No fracture occurred on the back side of this panel at this location. Unlike the 20-ply panel, there is no significant strain generated from the blast from the shape charge prior to impact. This is likely due to the differences in panel orientation. As shown in the figure, at the point of maximum deformation the panel undergoes a maximum strain of approximately 1.5 percent without fracture.

5.4 Summary of Posttest Analysis

The DIC results provide useful data for developing and validating computational models that simulate the impact of the blade on the shielding specimens and help to explain some of the mechanisms of failure. For the 20-ply panel deflections and strains up to the point of failure are provided. More information can be obtained from results from the 24-ply panel test. At the point of maximum deflection, the 24-ply panel sustained a maximum in-plane strain of approximately 1.5 percent without failure, whereas for the 20-ply panel the maximum in-plane strain was approximately 1 percent at the time of penetration. It was not possible with the DIC system to measure out of plane strains. The results indicate a highly dynamic event, with wave generation and fixture movement. The maximum radial displacement in the 24-ply panel is approximately 2.6 in. relative to the average displacement of four points at the corners of the specimen. The overall maximum radial displacement, including frame movement is approximately 4.3 in. Displacements of points spanning the two cracks that formed on the back side of the specimen indicate that the crack that initiated at the fixture frame was a result of transverse tension strains, while the crack that developed in the middle of the panel initiated in a region that was displacing radially outward and was a result of transverse compression strains resulting from the dynamic wave propagation in the panel.

6.0 Conclusions

The testing described in this report validated the results of the NASA LS–DYNA shielding design analysis. The results of the testing correlate very well with the NASA analysis results that predicted a penetration threshold between 20 and 24 plies of composite material for the open-rotor composite shield impact test. In addition, the test provided data on global deformation of the composite panels and local stress concentration leading to crack initiation. The blade release in the test occurred nearly as planned except that a NASA review of the blade trajectory determined that the blades impacted further forward than predicted because of the aerodynamics of the spinning blade not being taken into account.

Since the intent of this test was to validate the NASA analysis, the test utilized the boundary conditions specified in the analysis. This test demonstrated that a relatively low-weight solution may be possible for open-rotor fuselage shielding and also validated tools that can be used to evaluate potential designs. The test also demonstrated the importance of considering local high-strain effects during impact that can lead to crack initiation away from the impact site.

Numerical methods previously developed and the experimental methods described in this report provide tools that can be used for development and validation of future open-rotor fuselage shielding designs.

7.0 Recommendations

The results of this testing indicate that the NASA analysis methodology is a good tool to evaluate the use of barriers to protect the fuselage from uncontained blades. Additional investigation should be conducted, as design concepts for open-rotor aircraft emerge, to investigate the feasibility of protecting the fuselage from blades or blade fragments from these large rotors.

Appendix A.—Open-Rotor Protective Shield Study

The Naval Air Warfare Center Weapons Division (NAWCWD) was tasked under the Federal Aviation Administration's (FAA's) Catastrophic Failure Prevention Program to conduct an open-rotor protective shield study using the FAA Penetration Equations developed for the Uncontained Engine Debris Damage Assessment Model. The objective of this effort was to define the fuselage skin thickness required to stop impact from open-rotor blades and blade fragments. The tasking required the definition of a generic high-wing aircraft configuration with an open-rotor propulsion system (Fig. 52). Several iterations of the study were conducted with the initial effort defining a 2- by 8-ft shield of uniform thickness. Follow-on efforts defined optimized shield configurations and explored different shield materials. Fuselage structure was not considered in this analysis.

Two generic blade configurations were used in this analysis (Fig. 53). An aluminum blade was used for reference purposes and a composite blade was defined to better represent current open-rotor configurations. The open-rotor system was sized based on input from industry (Table V). The blade parameters are provided in Table VI. The second rotor blade was roughly a 20-percent-scaled version of the first blade. Spacing between rotors was defined at 15 in. from rotor 1 centerline to rotor 2 centerline. The rotor-to-rotor distance for modern open-rotor engines was not publicly available when this work was initiated, so a distance similar to the 1980s unducted fan was used in this analysis. More recent information indicates that modern open-rotor engines have a rotor-to-rotor centerline distance 2 to 3 times that used in this analysis. This will increase shield area and weight beyond those published in this report.

Variables in the study included blade material, fragment size, fragment orientation, and fuselage material. Blade and fuselage materials investigated were aluminum, a general carbon fiber/epoxy composite, and a braided carbon/high-strength epoxy fiber composite. Analysis was conducted to define the shielding weight required to stop the blade fragments. Results are provided for several shield configurations: a 2- by 8-ft uniform-thickness shield, an optimized shield for each individual rotor, and an optimized shield for both rotors. Optimized shield dimensions are based on fore-to-aft trajectory spreads of ±3°. A summary of the initial uniform shield study is presented in Table VII. This table shows the skin thickness required to stop a full blade fragment at a 90° (edge on) impact orientation for the various blade and fuselage materials. The weights listed are for an individual side of the aircraft so total aircraft shield weight would be twice the presented value.

A follow-on study was conducted to assess an optimized shield weight for the generic composite fuselage shield configurations. For this study, the shield is defined by the material thickness beyond nominal (0.1 in.) needed to stop the blade fragment. Blade impact conditions (trajectory, impact obliquity, and fuselage curvature) play a significant role in this design. As impact obliquity angles increase, the line of sight thickness through the material increases so less material is needed to stop a given blade fragment. This concept also takes advantage of the close proximity of rotors 1 and 2, using only the thicker panel segment in the overlap area. An example of the optimized shield is provided in Figure 54. Study results are presented in Table VIII. The study investigated a generic composite fuselage with a composite blade fragment at a blade fore and aft trajectory limit of ±3°. Parameters included blade impact orientations of 0° (flat), 60°, and 90° (edge on); 1/3 blade fragment; and full-blade fragment for rotors 1 and 2.

A final iteration of the shield study was conducted with a new high-strength, fracture-tolerant braided-composite fuselage material (Table IX). The study parameters were the same as those used in the generic composite effort.

A shield of uniform thickness provides adequate protection at the cost of excess weight. An optimized shield significantly reduces excess weight and provides the same level of protection against the defined blade fragment. For the case of a full composite blade at 90° impact orientation, the generic composite shield of uniform thickness weighs 195.7 lb. By optimizing the shield thickness, the weight is significantly reduced to 65.8 lb, a 129.9-lb weight savings. Using higher strength materials provides added benefit. The braided-composite-optimized shield weighs 42.2 lb compared with the generic composite 65.8 lb, an additional 23.6-lb weight savings.

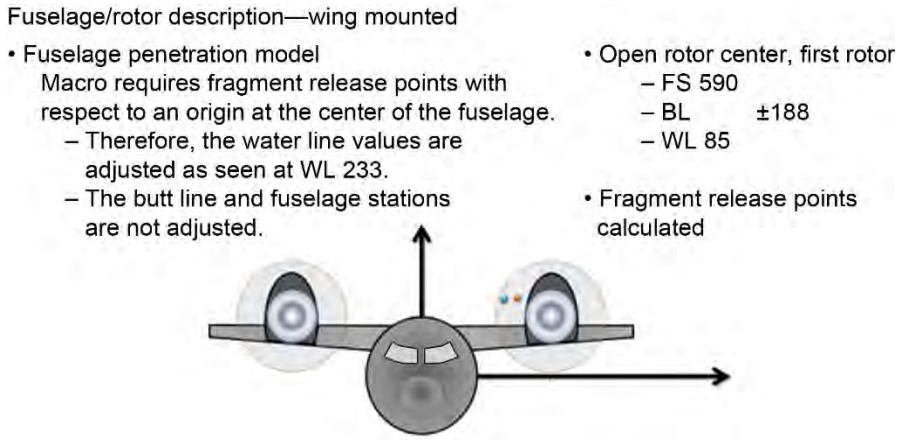

Figure 52.—Generic aircraft configuration with open-rotor system.

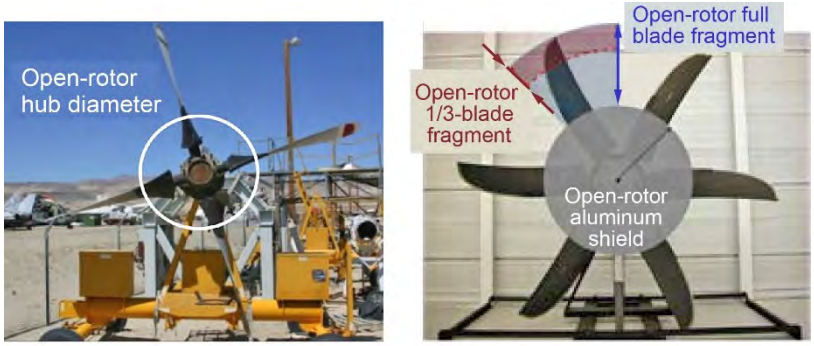

Figure 53.—Generic blade configuration for open-rotor system impact tests.

TABLE V.—OPEN-ROTOR FIRST ROTOR OVERALL CHARACTERISTICS

Diameter, ft	13.42
Blade length, ft	3.44
Hub diameter, ft	6.54
Rotor speed, rpm	1020

TABLE VI.—ROTOR BLADE GENERIC CONFIGURATIONS

	Aluminum blade		Composite blade	
	Rotor 1	Rotor 2	Rotor 1	Rotor 2
Full blade				
Length, ft	3.44	2.75	3.44	2.75
Width, ft	1.0	0.8	1.0	0.8
Average thickness, in.	0.8	0.8	2.0	2.0
Average skin thickness, in.	---	---	0.3	0.3
Weight, lb	39.6	25.3	17.0	10.8
Centroid radius, ft	4.93	4.64	4.93	4.64
Velocity, ft/s	527	497	527	497
1/3 Blade				
Length, ft	1.1	0.88	1.1	0.88
Width, ft	1.0	0.8	1.0	0.8
Average thickness, in.	0.3	0.3	0.3	0.3
Average skin thickness, in.	---	---	0.15	0.15
Weight, lb	4.68	3.04	2.7	1.7
Centroid radius, ft	6.71	6.16	6.71	6.16
Velocity, ft/s	647	594	647	594

TABLE VII.—UNIFORM-THICKNESS 2- by 8-FT SHIELD THICKNESSES AND WEIGHTS

[Rotor 1, full blade, 90° impact orientation.]

Blade material	Fuselage material		
	Aluminum	General composite	Braided composite
Blade 1			
Aluminum	1.414 in. 326.3 lb	1.483 in. 194.7 lb	1.145 in. 150.3 lb
Composite	0.886 in. 204.4 lb	0.929 in. 122.0 lb	0.717 in. 94.2 lb
Blade 2			
Aluminum	1.182 in. 272.7 lb	1.239 in. 162.7 lb	0.957 in. 125.7 lb
Composite	0.731 in. 168.7 lb	0.561 in. 73.7 lb	0.433 in. 56.9 lb

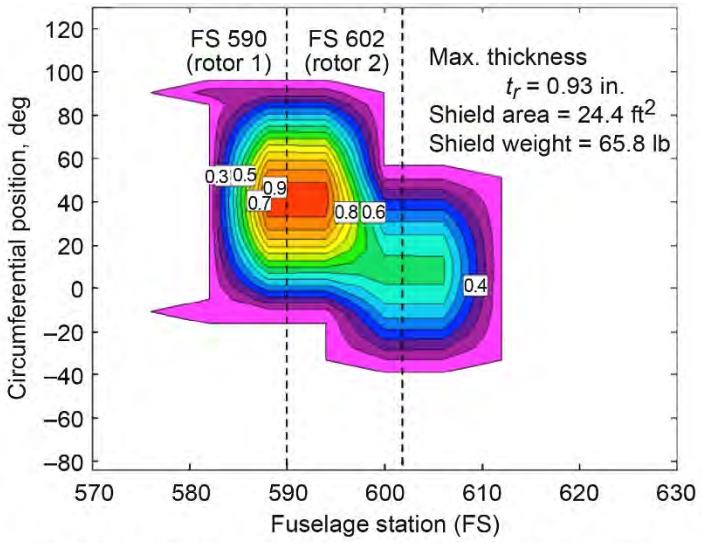

Figure 54.—Optimized shield thickness for case of composite blade and composite fuselage. Full blade impacting at 90° and trajectory limited to ±3°.

TABLE VIII.—OPTIMIZED SHIELD GENERIC COMPOSITE STUDY RESULTS

[Blade fore and aft trajectory limit of ±3°.]

Rotor	Fragment impacts on fuselage	Baseline fuselage results			Shielded fuselage optimized results				
		Fuselage weight, lb	Maximum residual velocity	Fragment penetration, percent	Fuselage weight, lb	Optimized shield weight, lb	Maximum required thickness, in.	Shielded area	
								$in.^2$	ft^2
(a) Full generic composite blade, composite fuselage									
Fragment impact 0°									
Combined rotors	104			51.9%		21.3	0.476	2632.2	18.3
Rotor 1	52	28.3	360.7	57.7%	42.5	14.2	0.476	1462.3	10.2
Rotor 2	56	30.5	247.1	42.9%	37.5	7.0	0.359	1169.9	8.1
Fragment impact 60°									
Combined rotors	104			59.6%		33.0	0.593	3022.1	21.0
Rotor 1	52	28.3	421.6	65.4%	50.3	22.0	0.593	1657.3	11.5
Rotor 2	56	30.5	319.6	50.0%	41.5	11.0	0.424	1364.8	9.5
Fragment impact 90°									
Combined rotors	104			69.2%		65.8	0.929	3509.6	24.4
Rotor 1	52	28.3	506.6	76.9%	74.0	45.7	0.929	1949.8	13.5
Rotor 2	56	30.5	446.1	57.1%	50.4	19.9	0.561	1559.8	10.8
(b) 1/3 generic composite blade, composite fuselage									
Fragment impact 0°									
Combined rotors	101			41.6%		8.1	0.337	2047.2	14.2
Rotor 1	52	28.3	312.9	46.2%	33.9	5.6	0.337	1169.9	8.1
Rotor 2	52	28.3	245.4	34.6%	30.8	2.5	0.276	877.4	6.1
Fragment impact 60°									
Combined rotors	101			47.5%		13.3	0.389	2339.7	16.2
Rotor 1	52	28.3	412.7	50.0%	36.9	8.6	0.389	1267.3	8.8
Rotor 2	52	28.3	342.3	42.3%	33.0	4.6	0.318	1072.4	7.4
Fragment impact 90°									
Combined rotors	101			55.4%		23.4	0.482	2729.7	19.0
Rotor 1	52	28.3	579.8	57.7%	42.7	14.4	0.482	1462.3	10.2
Rotor 2	52	28.3	502.0	50.0%	37.3	8.9	0.394	1267.3	8.8

TABLE IX.—OPTIMIZED SHIELD BRAIDED COMPOSITE STUDY RESULTS

[Limit trajectory to ±3°.]

Rotor	Fragment impacts on fuselage	Baseline fuselage results			Shielded fuselage optimized results				
		Fuselage weight, lb	Maximum residual velocity	Fragment penetration, percent	Fuselage weight, lb	Optimized shield weight, lb	Maximum required thickness, in.	Shielded area	
								$in.^2$	ft^2
(a) Full generic composite blade, braided composite fuselage									
Fragment impact 0°									
Combined rotors	104			44.2%		10.2	0.368	2242.2	15.6
Rotor 1	52	28.3	333.5	50.0%	35.8	7.5	0.368	1267.3	8.8
Rotor 2	56	30.5	206.1	35.7%	33.2	2.7	0.277	974.9	6.8
Fragment impact 60°									
Combined rotors	104			51.9%		18.3	0.458	2632.2	18.3
Rotor 1	52	28.3	402.8	57.7%	41.3	13.0	0.458	1462.3	10.2
Rotor 2	56	30.5	286.9	42.9%	35.7	5.2	0.327	1169.9	8.1
Fragment impact 90°									
Combined rotors	104			62.5%		42.2	0.717	3168.3	22.0
Rotor 1	52	28.3	498.1	71.2%	58.8	30.5	0.717	1803.5	12.5
Rotor 2	56	30.5	423.5	50.0%	42.0	11.5	0.433	1364.8	9.5
(b) 1/3 generic composite blade, braided composite fuselage									
Fragment impact 0°									
Combined rotors	101			24.8%		2.0	0.26	1218.6	8.5
Rotor 1	52	28.3	248.5	34.6%	30.1	1.8	0.260	877.4	6.1
Rotor 2	52	28.3	122.6	15.4%	28.5	0.2	0.213	390.0	2.7
Fragment impact 60°									
Combined rotors	101			35.6%		4.9	0.301	1754.8	12.2
Rotor 1	52	28.3	359.1	42.3%	32.0	3.7	0.301	1072.4	7.4
Rotor 2	52	28.3	255.8	26.9%	29.5	1.2	0.246	682.4	4.7
Fragment impact 90°									
Combined rotors	101			47.5%		11.6	0.372	2339.7	16.2
Rotor 1	52	28.3	537.4	50.0%	35.9	7.6	0.372	1267.3	8.8
Rotor 2	52	28.3	438.9	42.3%	32.2	3.9	0.304	1072.4	7.4

Appendix B.—Cross-Engine Debris Study

The Naval Air Warfare Center Weapons Division (NAWCWD) was tasked under the Federal Aviation Administration's (FAA's) Catastrophic Failure Prevention Program to conduct an open-rotor cross-engine debris study. The study was to be conducted using a generic low-wing midsize commercial aircraft configuration (Fig. 55); however, the results could be applied to a high-wing configuration currently used in many turbopropeller airplane configurations. The objective was to determine the design space (rotor vertical position) available for an open-rotor configuration to meet a 1/40 (9° of circumferential exposure) minimization requirement for cross-engine debris.

The analysis was based upon using the inherent shielding provided by the fuselage to minimize the exposure of damage to the opposite engine following a blade release. The fuselage diameter is similar to a typical narrow-body turbofan-powered transport airplane such as the Boeing 737 or Airbus A320. The open-rotor engine diameters were selected based upon current conceptual engine designs. Two blade diameters were assessed. The baseline rotor system was 13.5 ft, and a second, longer blade configuration (16.5-ft diameter) was also assessed for comparison purposes. The two blade lengths and rotor parameters are defined in Table X. In the analysis, the vertical position of the rotor centerline was adjusted to the point where the blade fragment first intersected the second rotor. The rotor centerline height above fuselage centerline and circumferential release point were recorded. The rotor was then raised until the circumferential release point equaled the original release point plus 9°. Again the rotor centerline above fuselage centerline was recorded. This analysis was conducted for a 1/3-blade fragment and a full-blade fragment. The critical parameters for the analysis were the center of gravity (CG) locations for the 1/3- and full-blade fragments, fuselage height, and rotor centerline height.

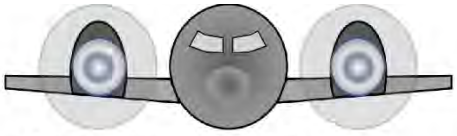

- Fuselage: 13 ft, 2-in.-vertical diameter
- Two rotor diameters assessed: 13.5 and 16.5 ft
- Initial spacing between the rotor tips and fuselage: 33.1 in.
- Rotors moved vertical to assess cross-engine debris scenarios

Figure 55.—Generic low-wing aircraft configuration.

TABLE X.—ROTOR DIMENSIONS USED IN CROSS-ENGINE DEBRIS STUDY

Dimension	Baseline blade	Larger blade
Diameter, ft	13.5	16.5
Diameter, in.	162	198
Tip radius, in.	81	99
Hub diameter, in.	79.50	79.50
1/3 blade length, in.	13.8	19.8
1/3 blade center of gravity (CG) radius, in.	74.1	89.1
Blade length, in.	41.25	59.25
Full blade CG radius, in.	55.0	79.0
Weight, lb	15.1	21.7

For the 13.5-ft-diameter system 1/3-blade analysis, the blade fragment initially impacts the second rotor when the rotor is raised 2 in. above fuselage centerline at a 359° release angle (Fig. 56).

The maximum vertical rise that still meets the 1/40 requirement is a 32.1-in. rotor height above fuselage centerline (Fig. 57(a)).

Analysis was conducted for the 13.5-ft-diameter rotor with a full-blade fragment. For the full blade, the initial impact to the second rotor occurs when the rotor is raised 11.5 in. above fuselage centerline. To meet the 1/40 requirement, maximum rotor system vertical rise could be up to 41 in. above fuselage centerline (Fig. 57(b)).

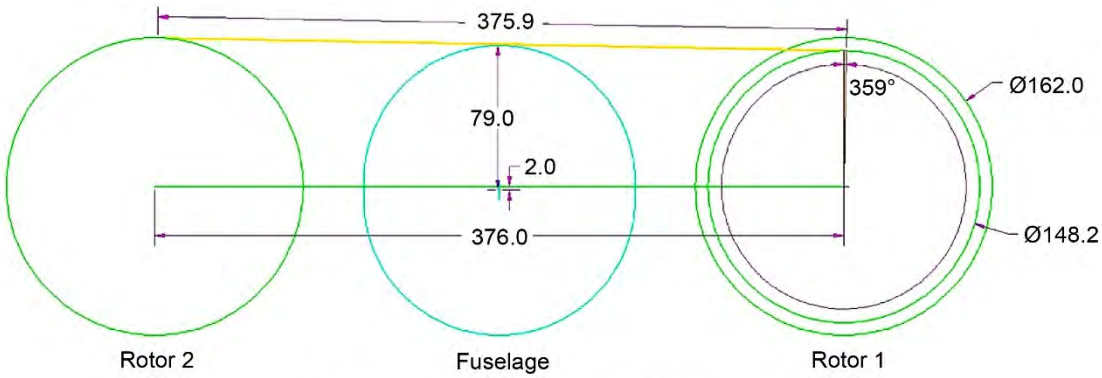

Figure 56.—13.5-ft-diameter rotor initial intersection.

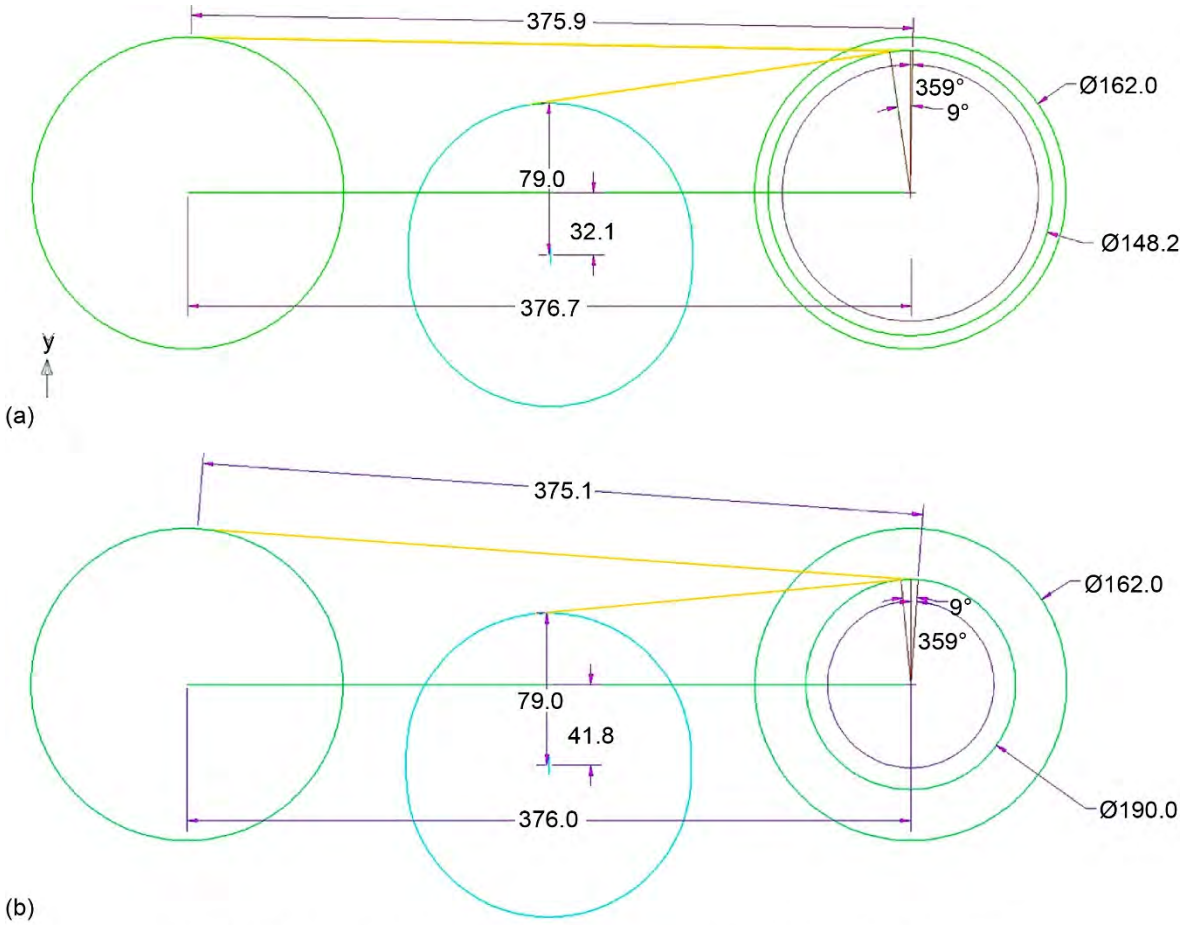

Figure 57.—13.5-ft-diameter rotor final positioning. (a)1/3 blade. (b) Full blade.

A second analysis was conducted with a 16.5-ft-diameter open-rotor system. With the larger rotor diameter (increased blade length) the design trade space is reduced to 18 and 23 in. from fuselage centerline for the 1/3-blade fragment and full-blade fragment, respectively (Fig. 58).

The objective of this analysis was to determine the design space (rotor vertical position) available for a low-wing open-rotor configuration to meet the 1/40 (9° of circumferential exposure) minimization requirement for cross-engine debris. Two rotor diameters were assessed—13.5 and 16.5 ft—and both systems had sufficient design space to meet the 1/40 cross-engine debris minimization requirement. As would be expected, the smaller diameter system had a larger trade space that met the requirement. A summary of results is provided in Table XI.

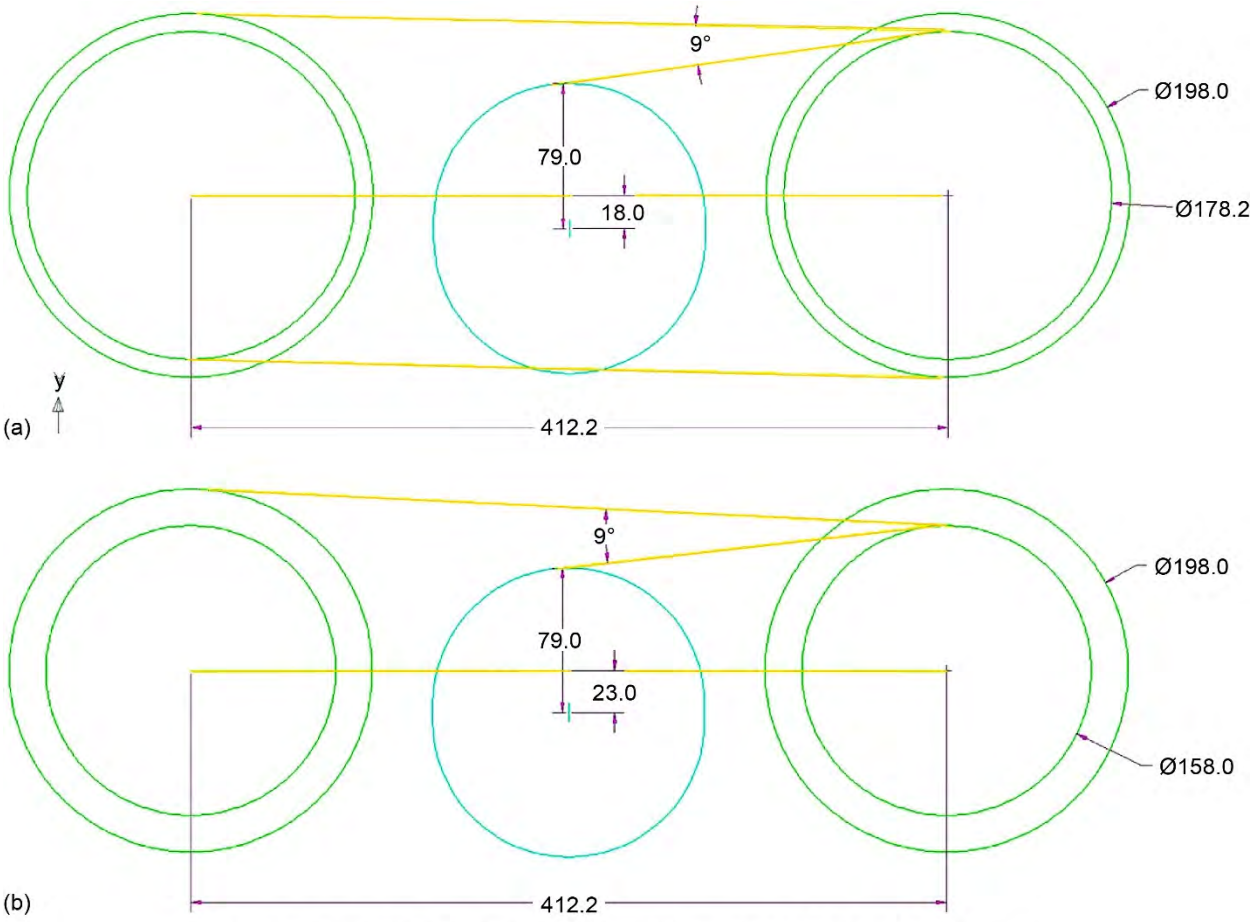

Figure 58.—16.5-ft-diameter rotor final positioning. (a) 1/3 blade. (b) Full blade.

TABLE XI.—RESULTS SUMMARY, ENGINE CENTERLINE VERTICAL TRADE SPACE AVAILABLE

Rotor diameter, ft.	1/3 blade, in.	Full blade, in.
13.5	32.1	41
16.5	18	23

Appendix C.—Test Stand Vibration Data

Six accelerometers were placed on each of the test stands supporting the test articles as previously described in Section 3.4. The intent of these accelerometers was to provide boundary condition information for future finite element analysis. In this appendix, digital image correlation (DIC) information is also provided to identify motion of the shields at the corners of the stand in addition to the accelerometer data.

The accelerometers were Dytran Instruments, Inc., 3200BST shock accelerometers with a maximum rating of 10 000 g, and a frequency range of 0.35 to 10 000 Hz. The locations and directions of the accelerometers are documented in Section 3.4.

Two sets of plots are provided, six for each shield to show the accelerations recorded during the test. Approximately 0.11 s of data was recorded at 100 000 samples per second for each channel. There is a significant difference in the level of the signals for the 20-ply panel and the 24-ply panel. In the test, the released blade impacted the frame of the 20-ply panel after penetrating the shield. This resulted in very high measurements on the 20-ply accelerometers and clipping on two of the channels. The 24-ply shield was not penetrated. The raw accelerometer data for the 12 accelerometers are shown in Figures 59 and 60 for the 20- and 24-ply panels, respectively. The acceleration response for the 12 channels begins with a low value prior to detonation of the charge releasing the two blades. After detonation there is an increase in response, likely due to the pressure pulse from the detonation. Impact of the blade occurs at approximately 0.018 s, when the acceleration increases dramatically and then gradually decreases to a low level at approximately 0.1 s.

The 20-ply frame data were compromised by the impact of the blade into the frame; therefore, no further processing was performed. For the reader's convenience, power spectral density (PSD) plots are provided for the 24-ply-frame accelerometers in Figure 61. There was measurable frequency content in all the signals up to approximately 25 KHz, well below the Nyquist frequency. Above that the signal magnitudes were low. Data are shown for the frequency range of 0 to 1000 Hz. The PSDs were calculated with MATLAB (The MathWorks, Inc.) using the script in Figure 62.

DIC was available during the test. In order to define the stand movement, the displacement was computed at a number of points on the perimeter of the 24-ply panel. The locations of points where displacements were measured are shown in Figure 63. The circumferential, axial, and radial displacements are provided for points 10 to 13 in Figures 64 to 67 for the four corners of the shield. The positive directions of axial and circumferential displacements are shown in Figure 63. Positive values of radial displacements are out of the page. In the plots, time 0 is the time of the first impact of the blade on the panel. This corresponds to a time of approximately 0.018 s in Figure 60. These displacements are located very close to the accelerometer locations. Computations were only possible up to 0.02 s after impact because of severe vibrations at the camera location making it impossible for the ARAMIS (GOM mbH, Germany) software to accurately track the pattern on the panel. Maximum displacement of the panel occurred at approximately 0.0065 s after impact, as shown in Figure 45.

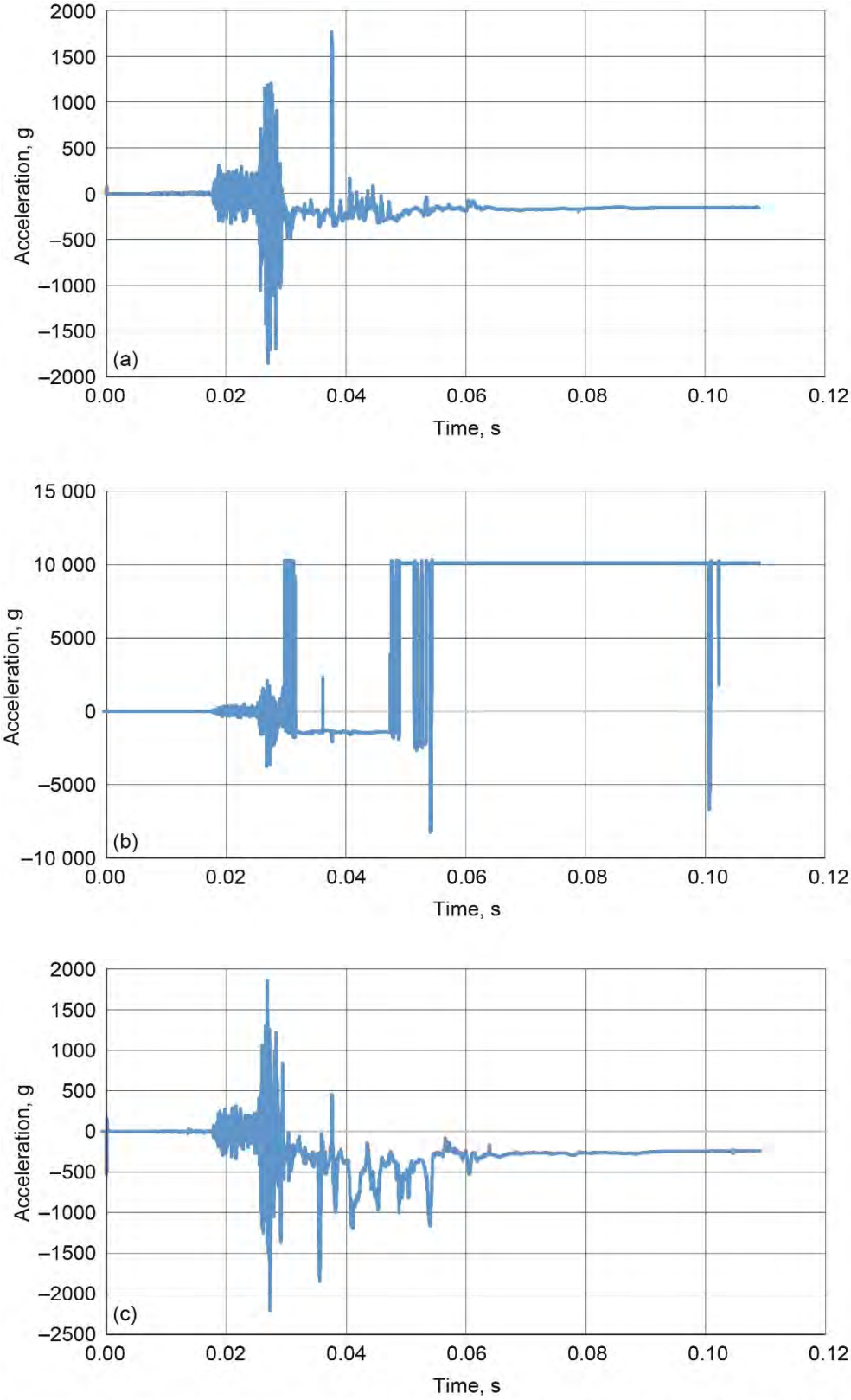

Figure 59.—Accelerometer response for 20-ply panel. (a) P20–X1. (b) P20–Y1. (c) P20–Z1.

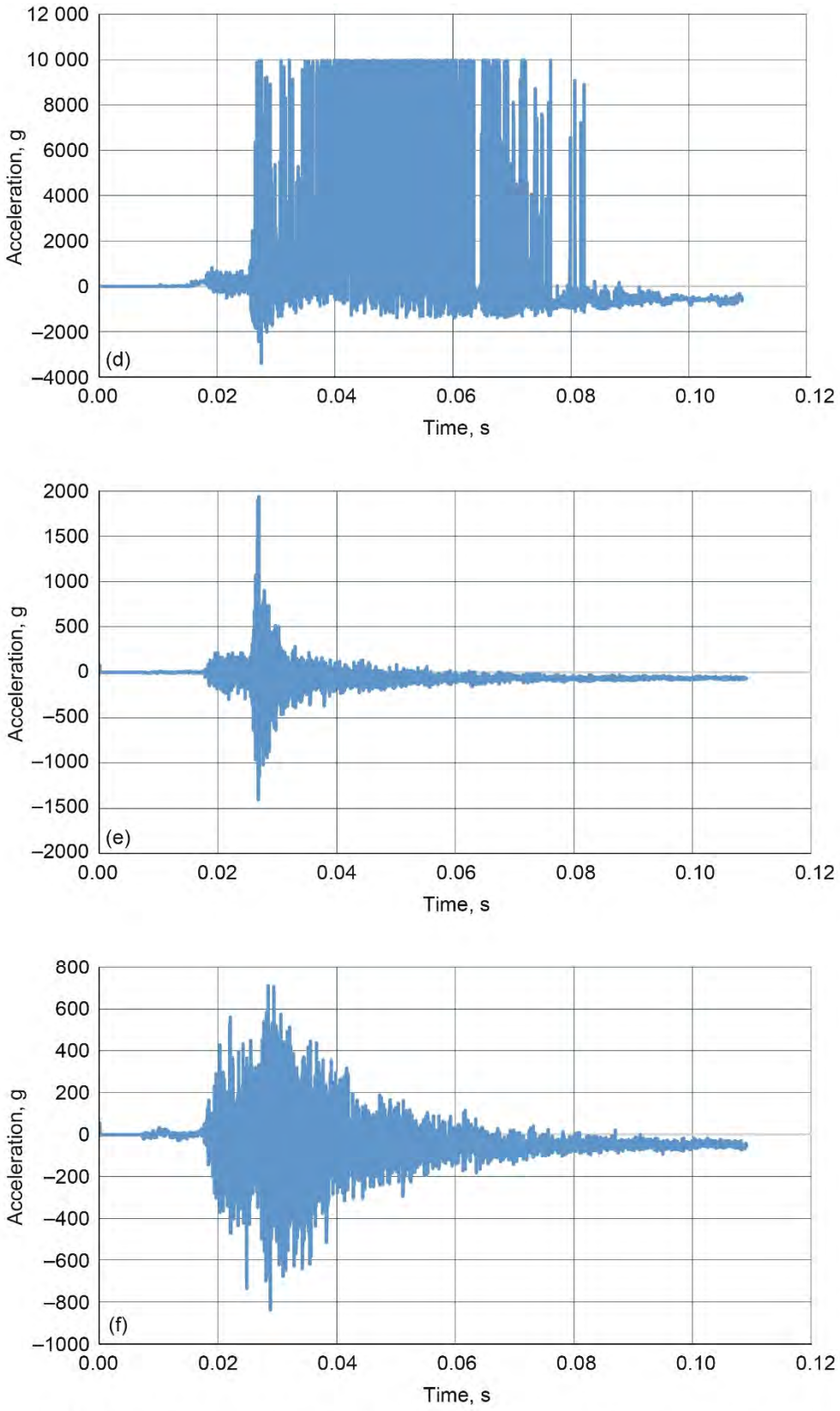

Figure 59.—Concluded. Accelerometer response for 20-ply panel. (d) P20–Y2. (e) P20–Z2. (f) P20–Y3.

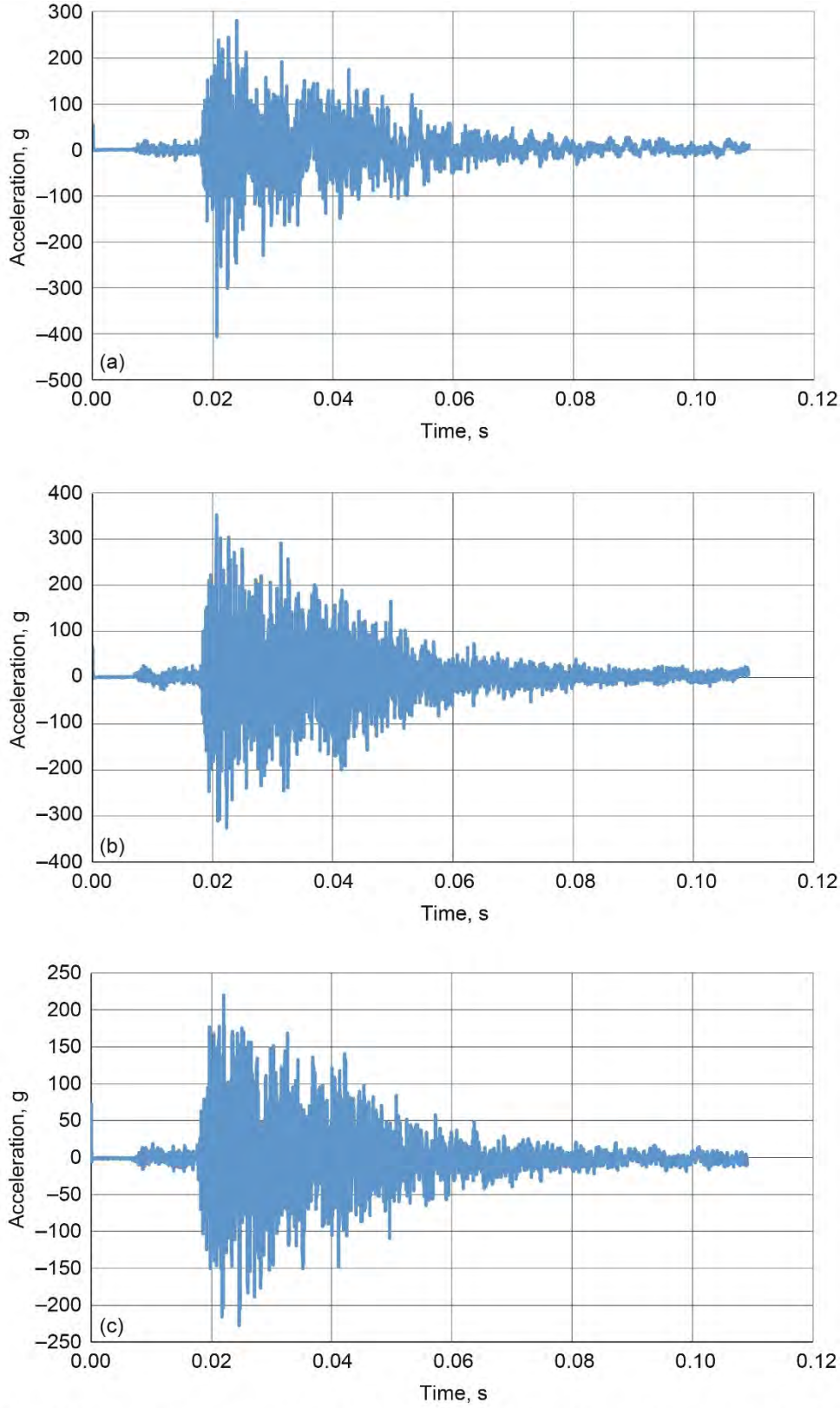

Figure 60.—Accelerometer response for 24-ply panel. (a) P24–X1. (b) P24–Y1. (c) P24–Z1.

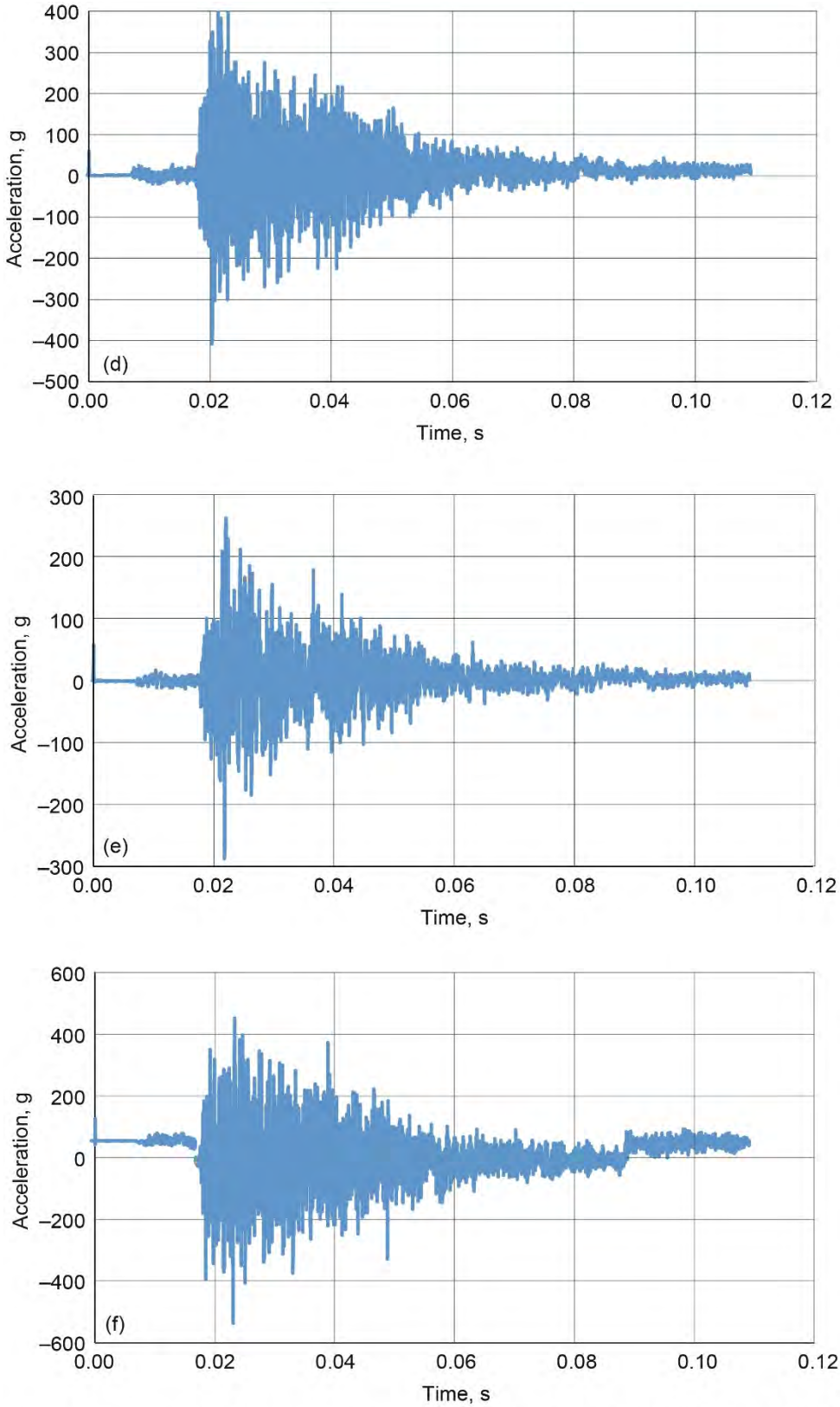

Figure 60.—Concluded. Accelerometer response for 24-ply panel. (d) P24–Y2. (e) P24–Z2. (f) P24–Y3.

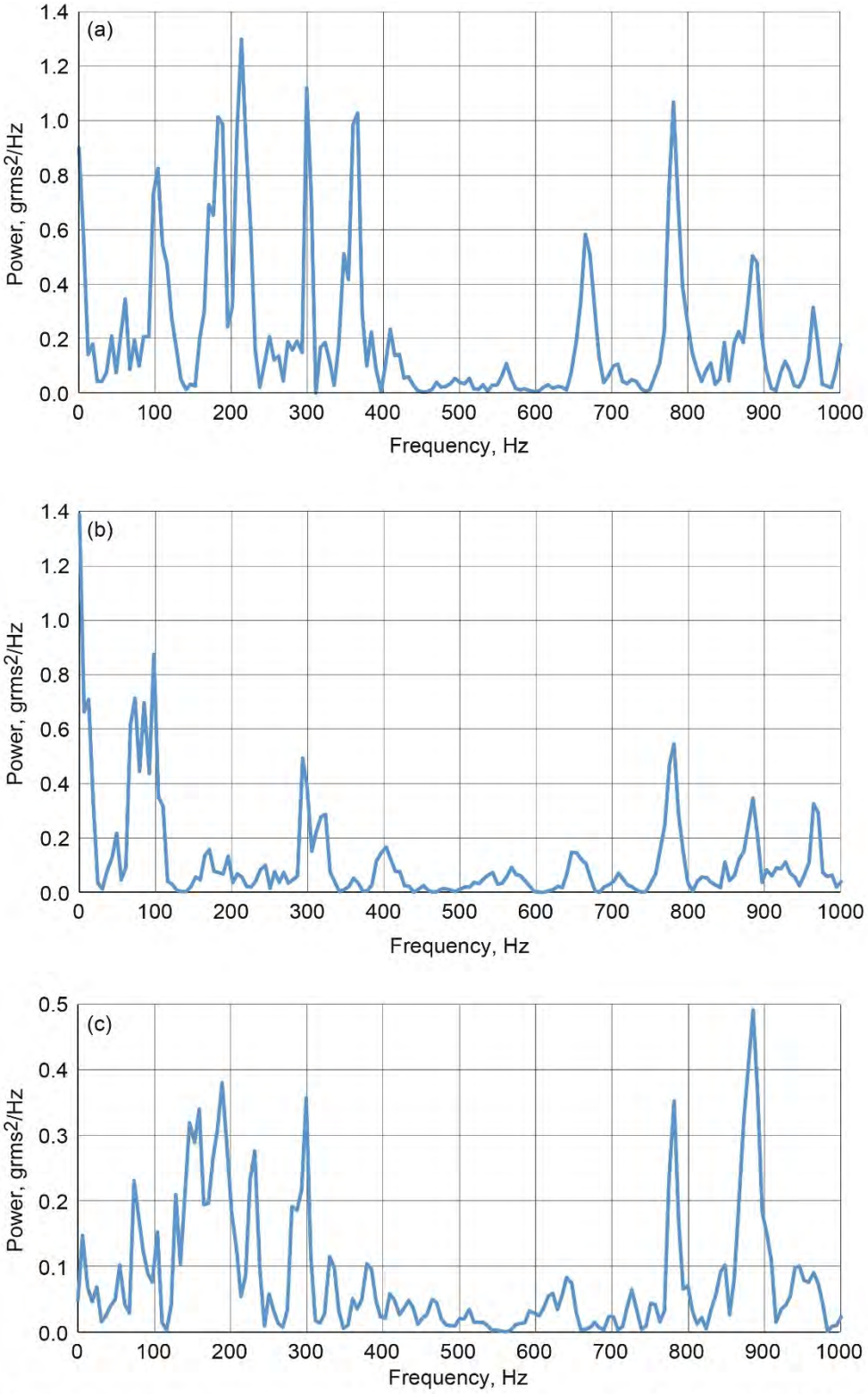

Figure 61.—Power spectral density of accelerometer responses for 24-ply panel. (a) P24–X1. (b) P24–Y1. (c) P24–Z1.

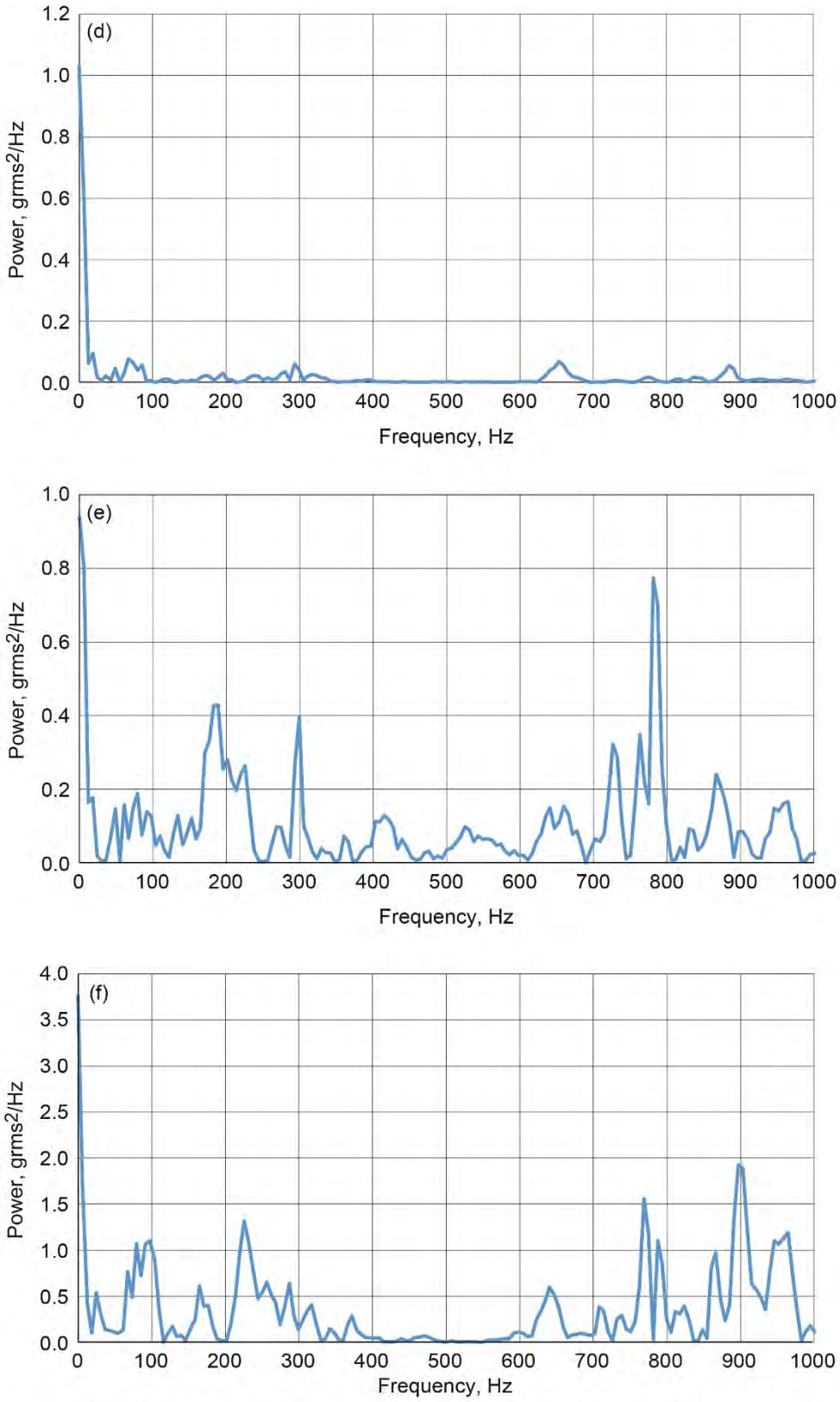

Figure 61.—Concluded. Power spectral density of accelerometer responses for 24-ply panel. (d) P24–Y2. (e) P24–Z2. (f) P24–Y3.

Contents


```
clear;
clc;
closeall;
```

Read in data

```
data = xlsread('zeroeddata time offset.xlsx');
cf = 9.81*1000/25.4;    % Conversion factor for acceleration of gravity in in/sec2;

t = data(:,1);
acceleration = data(:,10:15); %Select only signals from the 24 ply stand
```

Construct the signals

```
T = mean(diff(t));          % Sampling time
Fs = 1/T;                   % Sampling frequency
L = length(t);              % Length of signal
```

Determine the Power Spectral Density (frequency contributions. Units will be g(rms)^2/Hz.

```
NFFT = 2^nextpow2(L);% Next power of 2 from length of y
for i = 1:1:6
    Y = fft(acceleration(:,i),NFFT);
    Pyy(:,i) = (1/(Fs*NFFT)) * abs(Y).^2;
    Pyy(2:end-1, i) = 2*Pyy(2:end-1, i);
end

figure;
hold on;
plot(t, acceleration(:,2)/cf);
hold off;
f = Fs/2*linspace(0,1,NFFT/2+1);

for  j = 1:1:6
    Pyys(:,j)=Pyy(1:NFFT/2+1, j);
end
% Plot power spectral density.

figure('Units','normalized','Position',[0.35 0.1 0.3 0.4]);
hold on;

plot(f, Pyy(1:NFFT/2+1,2));

xlabel('Frequency (Hz)');

ylabel('Power Spectral Density');
hold off;
```

Published with MATLAB® R2014b

Figure 62.—Script for computing power spectral density.

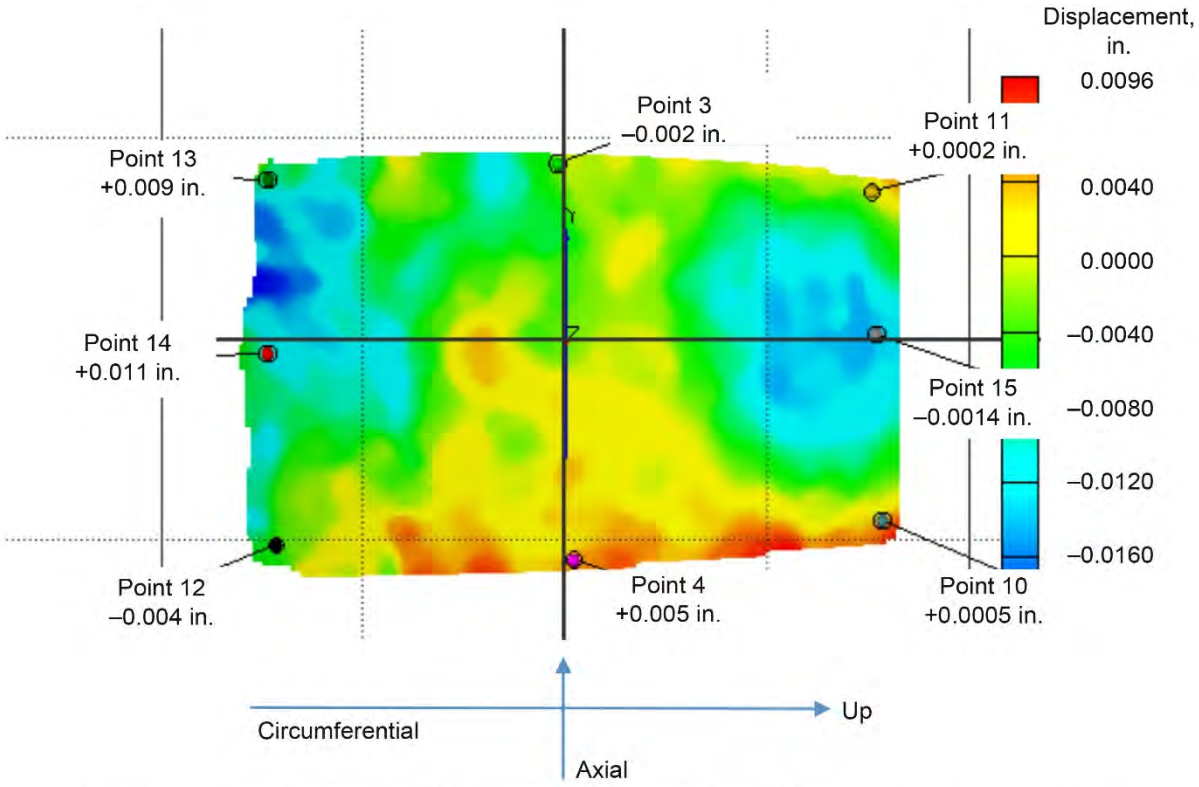

Figure 63.—View of back side of 24-ply panel showing locations of four points near corners where displacements were computed. Upward direction is to right.

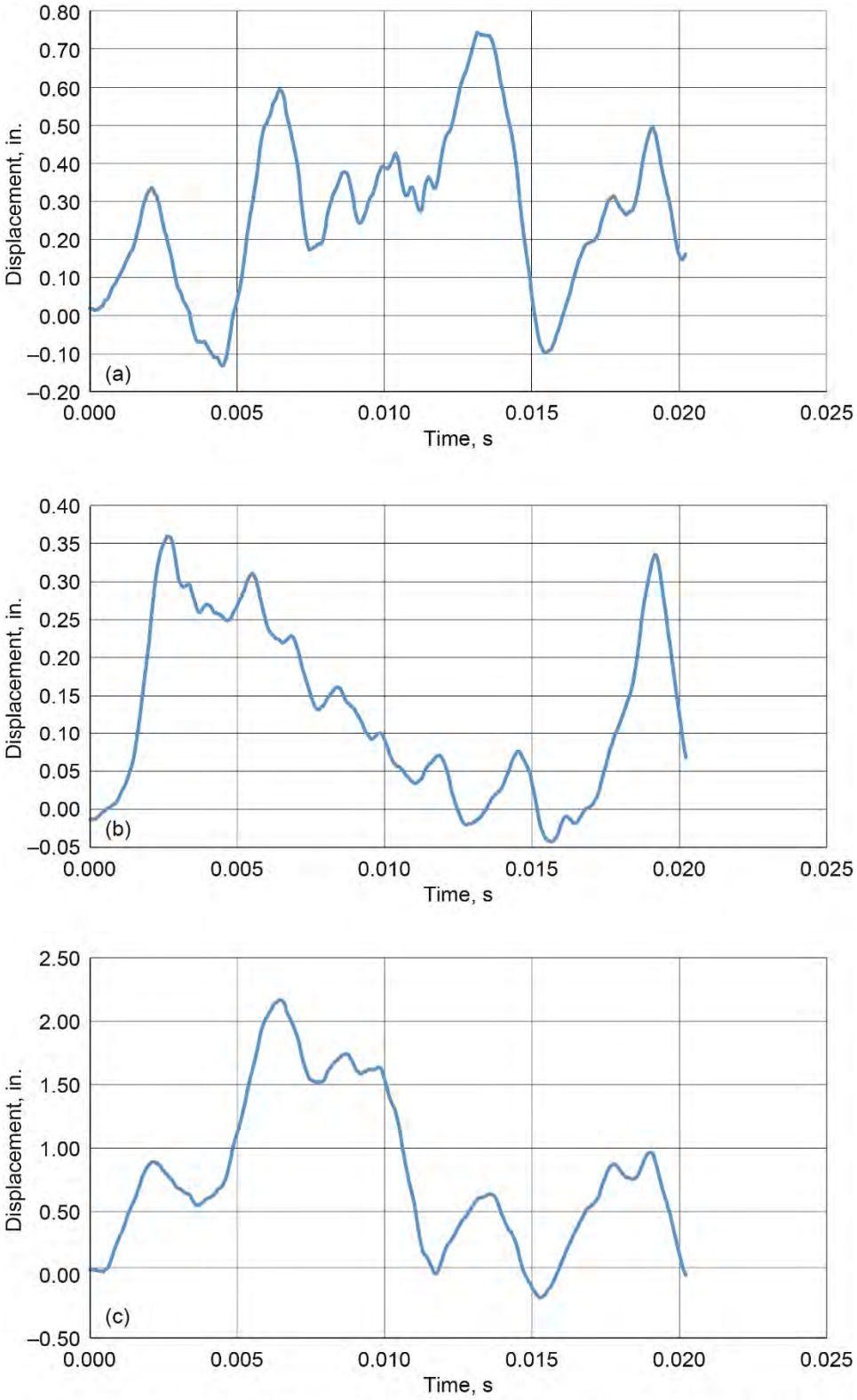

Figure 64.—Displacement of point 10 (see Fig. 63) on 24-ply panel. (a) Circumferential. (b) Axial. (c) Radial.

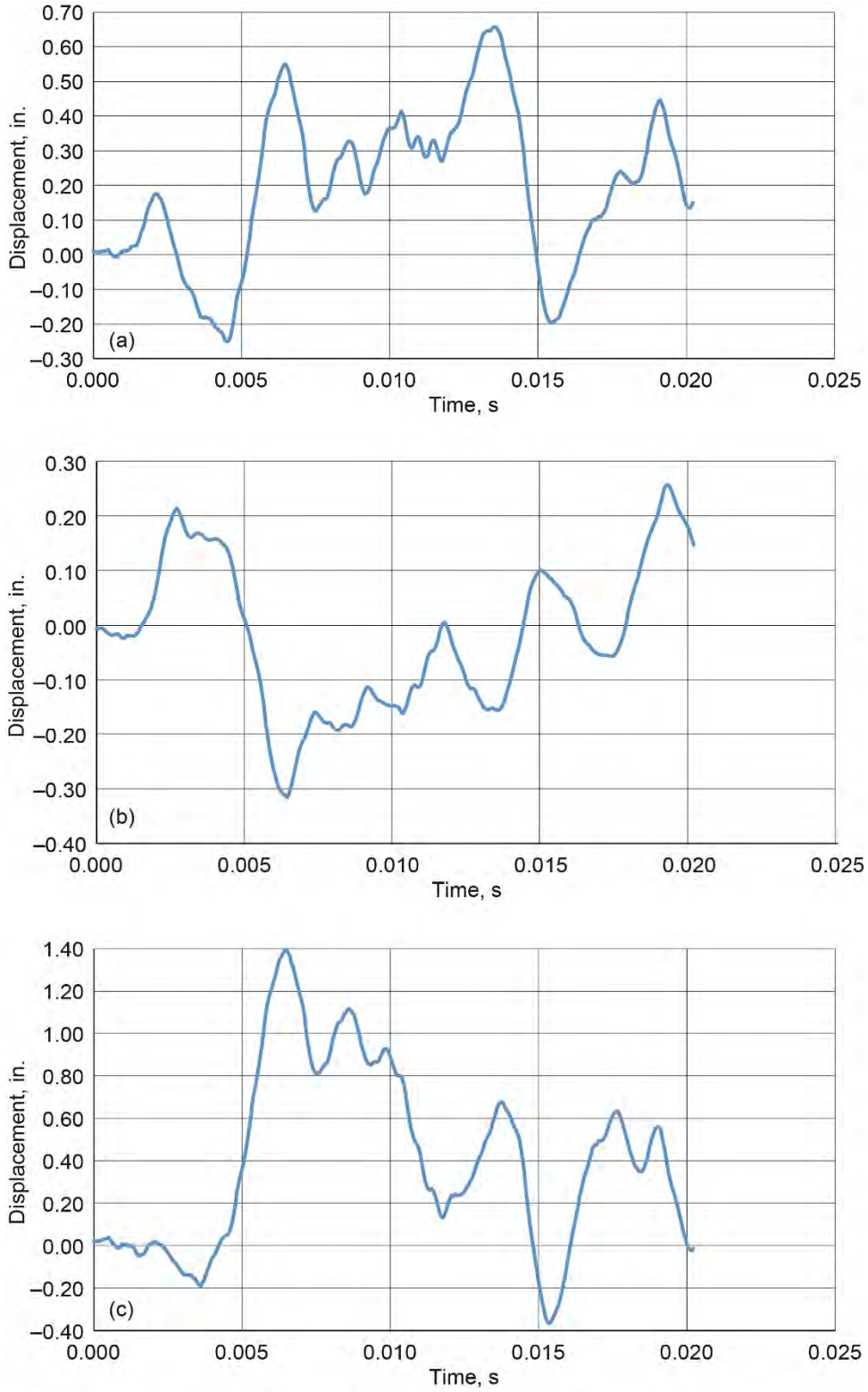

Figure 65.—Displacement of point 11 (see Fig. 63) on 24-ply panel. (a) Circumferential. (b) Axial. (c) Radial.

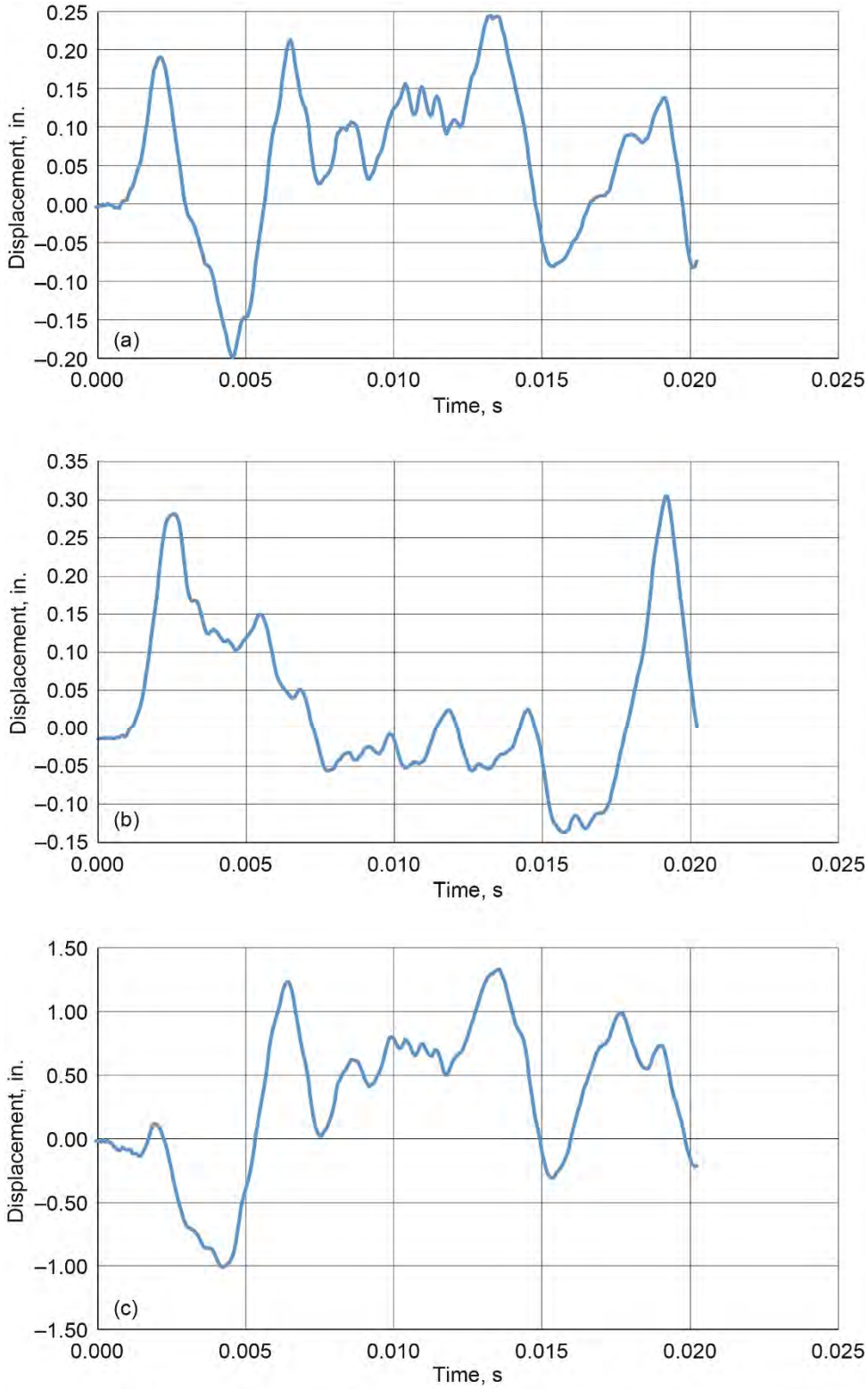

Figure 66.—Displacement of point 12 (see Fig. 63) on 24-ply panel. (a) Circumferential. (b) Axial. (c) Radial.

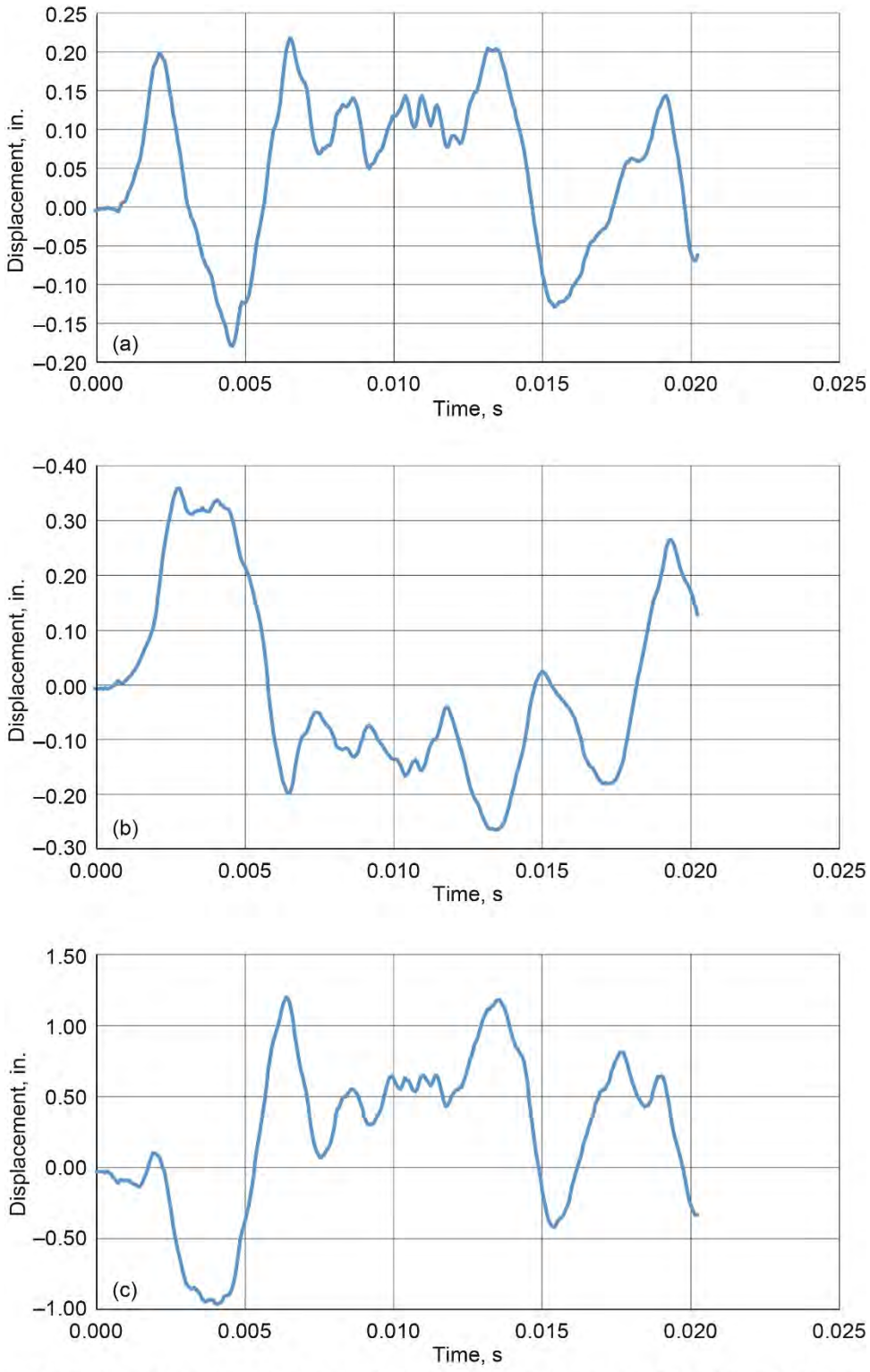

Figure 67.—Displacement of point 13 (see Fig. 63) on 24-ply panel. (a) Circumferential. (b) Axial. (c) Radial.

References

1. Carney, Kelly, et al.: Weight Assessment for Fuselage Shielding on Aircraft With Open-Rotor Engines and Composite Blade Loss. NASA/TM—2013-216582 (DOT/FAA/TC–13/34), 2013.
2. Sweetman, Bill: The Short, Happy Life of the Prop-fan. Air & Space Magazine. 2005. http://www.airspacemag.com/history-of-flight/the-short-happy-life-of-the-prop-fan-7856180/#ixzz33gvo7PuE Accessed June 10, 2015.
3. Bowman, C.L., et al.: Mechanical Properties of Triaxial Braided Carbon/Epoxy Composites. NASA Document ID 20040112004, 2003. http://ntrs.nasa.gov